Cover page

Handed in by

Mirjam Martina Läderach
vxf152@alumni.ku.dk

Hand-in information

Titel: Master Thesis Mirjam Läderach

Continuous flow analysis on EastGRIP ice core:

Optimization of optical dye method and results from acidity measurements on the EastGRIP ice core

Master Thesis
MSc in Climate Change

Mirjam Läderach
vxf152@alumni.ku.dk

Physics of Ice, Climate and Earth

Niels Bohr Institute

Faculty of Science

University of Copenhagen

Supervision: Helle Astrid Kjær and Paul Travis Vallelonga

Submission date: 31 May 2019

Abstract

This study presents continuous flow analysis (CFA) acidity data obtained from the EastGRIP ice core and contributes to the climate record of past volcanic activity. A restructured setup for the optical dye acidity technique developed by Kjær et al. (2016), enabling a lower signal to noise ratio, is presented and evaluated. Within this new setup, the optimal concentration of the two pH-indicator dyes bromophenol blue and chlorophenol red for the reagent used in this technique is assessed and estimated at 0.04 mg/mL to 0.06 mg/mL. Further, the method is applied to the EastGRIP ice core section of 350.35 m to 904.75 m depth, roughly corresponding to a time range spanning from 3 ky to further than 7.6 ky before 2000 CE. The evaluation of the standard data from this ice core section concludes that the EastGRIP acidity data obtained as part of this study is of reasonable quality and can thus be trusted in future investigations of climatic events. To this end, a selection of the EastGRIP measurement data for acidity combined with CFA meltwater electrolytic conductivity, dust, calcium and ammonium data, showcases selected indications for volcanic activity at the time.

Acknowledgements

Contents

Figures

Tables

1. Introduction

Anthropogenic climate change is clearly detectable and attributable: It is estimated that human activities have already led to approximately 1.0 °C global warming above pre-industrial levels, with human activities as the dominating cause for the observed increase of global average surface temperature. The rate and global scale of the anthropogenic impact on the climate system is unprecedented and causes long-term changes of the Earth's climate system (IPCC 2013a, IPCC 2018). Climate change is one of the most pressing environmental problems of our time. But still – as can be seen as one of the most alarming aspects with regards to our changing climate – the uncertainty about both the nature and rate of projected climate change are vast.

To this end, studying past climates facilitates the understanding of how the climate may respond to future changes in different forcings (Richardson et al. 2011). Paleoclimatology investigates the climate prior to the instrumental period: By using proxies for various signals, it entails the reconstruction of past natural climatic variations and their causes. Paleoclimatic data and modelling provide quantitative information on different external forcings, such as the sun, volcanoes and orbital parameters, and on changes in the atmospheric composition that exert an influence on the Earth system. In fact, records of past climatic conditions and forcings are recorded in natural archives, such as loess, marine and lake sediments, corals, speleothems or ice (Bradley 2015, IPCC 2013b).

Ice cores from polar areas constitute important archives as they store both local and global climate parameters in high resolution and date back far in time, covering past glacial and interglacial periods. This study investigates the mid-Holocene climate record in the Greenland EastGRIP (East Greenland Ice-core Project) ice core. Through accumulation of snowfall over the Greenlandic and Antarctic ice sheets and the subsequent metamorphism of snow crystals to firn and ice, a unique record of paleoclimatic information is formed. Ice cores date back 130,000 and more than 800,000 years to this date in Greenland and Antarctica respectively (Bradley 2015, Svensson 2014). Indeed, ice cores comprise a vast amount of information: on past temperatures, volcanism, solar activity, dust, biomass burning and the past atmospheric composition including the concentration of greenhouse gases, just to name a few

(Svensson 2014). Ancient air is preserved in trapped air bubbles and can be analyzed for trace gases like carbon dioxide (CO_2) and methane (CH_4). Furthermore, impurities in the ice, such as aerosols and water-soluble gaseous elements, are preserved in the surrounding ice. This area of study – glaciochemistry – analyzes the chemical compositions of impurities in solid precipitation accumulated on ice sheets and provides a unique tool for interpreting the composition of the atmosphere in the past (Legrand and Mayewski 1997). Some of these impurities originate from volcanoes. Large eruptions inject sulfur gases into the stratosphere, which are precipitated over the polar caps, leading to an acidic layer in the ice that indicates volcanic activity at the time (Cuffey and Paterson 2010).

Volcanic eruptions have a significant impact on the Earth's climate on different time scales. An impressive example constitutes the 1815 Tambora eruption that led to the later called "year without a summer" in 1816 that inspired writer Mary Shelley's tale of Frankenstein (Robock 2000). Thereby, the high amounts of sulfur compounds ejected into the stratosphere during volcanic eruptions are the dominant cause for natural climate change on the annual and multi-decadal time scale and explain much of the climate variability in the pre-industrial era of the last millennium (IPCC 2013c). Understanding of such natural climate fluctuations caused by volcanism in the past facilitates detection of global warming since industrialization and attribution to anthropogenic greenhouse gas emissions. Furthermore, through the use of data on past volcanic eruptions, climate models used for projecting anthropogenic effects on the climate can be built and improved. Additionally, volcanic events are used extensively for dating and cross-dating ice cores, when precise dates can be assigned to the respective eruptions (Robock 2000, Kjær 2014). There is yet no complete record of past volcanism, though, this study tries to contribute to this field of study.

The aim of this study is to investigate volcanic activity in the EastGRIP ice core data with an optimized acidity technique and to support the completion of the climate record of the mid-Holocene period. This study follows three main objectives: First, this study optimized the continuous flow analysis (CFA) technique used for measurement of acidity in ice cores developed by Kjær et al. (2016). Thereto, the setup was changed in order to increase the signal to noise ratio, and a dye concentration test was performed, aiming at optimizing the concentration of the dye reagent used for this optical dye method. This study evaluates the optimization of the changed method setup and of the

dye concentration of the reagent. The optimized acidity method setup was then used on the EastGRIP ice core during the measurement campaign 2019 in Berne, Switzerland. To this end, as a second step, this study evaluates the performance of the optimized acidity method over the course of the EastGRIP measurement campaign 2019. And third, the study investigates volcanic activity in the EastGRIP ice core data, thereby supporting the completion of the climate record of the mid-Holocene period: While chemistry records have been obtained for most of the NEEM (North Greenland Eemian Ice Drilling) ice core dating back to the last interglacial period, the Eemian, the NEEM brittle layer in the mid-Holocene between 609 m and 1281 m depth remains an area of discontinued data (Neff 2014). The acidity measurements of the EastGRIP core are showcased in comparison to the meltwater electrolytic conductivity, dust and ammonium data, providing insight into the state of the climate at that time and pointing towards interesting areas of future research with this data set.

This paper will first introduce its theoretical background, covering ice cores as a climate archive and the chemical analysis of impurities in ice cores (chapter 2). Further, chapter 3 outlines the impact of volcanic eruptions on the climate and acidity as a proxy for volcanic activity. Chapter 4 then reports the methodological procedure used in this study to obtain the above-presented objectives. The results are presented and discussed in the results chapter (5) and set into a broader context in the chapter 6.

2. Glaciochemistry

Ice cores provide a high-resolution archive, recording past environmental and climatic conditions covering approximately the last 130,000 years in Greenlandic deep ice cores and 800,000 years in Antarctic counterparts (Bradley 2015, Svensson 2014). Thereby impurities in the ice core, in theory, offer an insight into the past atmospheric composition and circulation. To this end, this chapter introduces the chemical analysis of impurities in ice cores in the context of ice cores as a climate archive with a specific focus on the EastGRIP ice core analyzed in this project.

2.1 Ice cores as climate archives

Polar ice is of particular interest. First, the relative remoteness of both the Antarctic and the Greenlandic ice sheets provide the cleanest atmospheric environments for the Northern and Southern Hemisphere. Second, the meteorological conditions are characterized by a distinct seasonal cycle with a long polar night, very cold temperatures and subsequent high dryness of the air leading to low reactivity of the atmosphere. Third, and most importantly for this study, the solid precipitation accumulating on the polar ice caps enable the reconstruction of past atmospheric chemistry and thus the Earth's past climate. This feature, however, comes with uncertainties linked to the relation between the composition of the atmosphere and the precipitation (Legrand and Mayewski 1997).

Over time periods of hundreds of thousands to millions of years, snow is accumulated on the Greenlandic and Antarctic ice sheets and through the subsequent metamorphism of snow crystals to firn and ice by means of increasing compression, a unique record of paleoclimatic information is formed. Samples of this archive, ice cores, hold an abundance of information of high resolution (Legrand and Mayewski 1997).

New studies show that the Greenlandic ice sheet has been growing on bedrock and mountains over the last 1 to 7.5 million years (Bierman et al. 2016, Schaefer et al. 2016). Unless there are internal deformations taking place, the accumulation process ensures that the snow and later, the ice is in chronological order with the oldest ice at the bottom of the ice sheets. With the increasing weight of the overlying ice, and the stretching due to the flow of the ice towards the ice sheet margins, the annual layers are thinning towards the bedrock. Ideal areas for ice drilling are thus areas where the ice is

stretched only horizontally and where there is no surface melting that blurs the record; this is the case for the central part of an ice sheet (Cuffey and Paterson 2010).

Among other methods at hand, the age of the ice can be determined with a combination of layer counting and ice flow; ice flow modeling comes into use when distinct annual layers are not discernible. Properties that portray an annual variability, as for example impurities of nitrate, hydrogen peroxide, calcium or ammonium, the ratio of oxygen and hydrogen isotopes or the concentration of microparticles, can be used for layer counting. Manual or computer assisted layer counting, however, is only possible in areas with sufficient snow accumulation and if the risk of zero snowfall in one year is close to zero (Cuffey and Paterson 2010, Legrand et al. 1997). When annual accumulation rates are high enough, annual layers can be detected up until around 60'000 years back, as is the case for Greenlandic ice cores. After that the annual layers cannot be identified due to the advanced thinning of the ice (Bradley 2015, Svensson et al. 2008). Numerous well-dated marker horizons have been defined in the ice, for example tephra or acid layers. For example, the Tambora eruption 1815 CE has been identified in several ice cores. These marker horizons help to constrain the depth-age relation in the ice and can be used for synchronizing different ice cores with each other (Cuffey and Paterson 2010, Svensson 2014).

The ice cores contain a wealth of information: First of all, the stable isotopic $^{18}O/^{16}O$ and D/H composition of the ice offers a temperature record of the air mass the snow precipitated from, thus serving as a local temperature proxy. Moreover, the ice contains small quantities of impurities – soluble, insoluble and gaseous – that reflect the past composition of the atmosphere (Cuffey and Paterson 2010, Legrand and Mayewski 1997).

Past concentrations of atmospheric trace gases can be measured in the gas component of ice cores. Over the course of the different stages of firn compaction, the atmospheric gases get trapped in bubbles in the ice core in the close-off zone. Subsequently, the gases transform into clathrates with increasing depth and pressure. Thus, by sampling these bubbles, past concentrations of atmospheric gases can be directly measured; this is fundamental for understanding the terrestrial climate, as some of them – CO_2, CH_4, and other greenhouse gases – play the key role in regulating today's climate (Cuffey and Paterson 2010, Legrand and Mayewski 1997). Direct CO_2 measurements from ice cores are, however, only trusted in Antarctic ice cores. It is believed that chemical reactions in

the ice due to higher impurities in Greenland lead to an in situ production of CO_2. The exact reaction mechanism, however, is not yet understood (Anklin et al. 1995, Oeschger et al. 1988, Kjær 2014).

Furthermore, aerosols and water-soluble impurities are either directly deposited on the ice sheet surface or captured during the process of cloud droplet and ice crystal formation. The chemical analysis of these impurities is called glaciochemistry and will be more thoroughly examined in section 2.2 (Legrand and Mayewski 1997).

It is important to take into account that the measured climate signals themselves are not free from perturbation: With a changing climate, precipitation rates and temperature have been changing over time, affecting the measured climate proxy recorded in the ice. So, the precipitation rate determines the rate at which gases are enclosed in the form of bubbles. Moreover, changing precipitation rates affect the ratio of wet and dry deposition of particles. Changes in temperature can cause melt layers in the ice; these in turn influence the close-off depth of bubbles and in severe cases may melt away entire years, or redeposit the information in deeper areas of the ice, which impedes the dating of the ice. Additionally, changes in temperature can lead to alterations of the chemical composition of the ice (Kjær 2014).

2.2 Impurities in ice cores

Impurities in the ice, in theory, offer an insight into the past atmospheric composition and circulation. Their record in the Antarctic and Greenlandic ice sheets provides unique information on the past climate of the respective hemisphere, as they are not globally mixed in the atmosphere due to their atmospheric residence time on the scale of days to weeks. A lot of factors play into the formation of this climate archive, such as the geographical location and strength of the impurities' source, atmospheric processes, the incorporation of the impurities into the ice as well as processes altering the chemistry post-deposition. These have to be taken into account and extenuate the interpretation of the record (Cuffey and Paterson 2010).

Sources of the impurities comprise terrestrial dust, the ocean surface, biological activities and – in more recent history – increasingly anthropogenic pollution. Particulate impurities are microparticles of a typical size of 0.1-5 μm, transported in the atmosphere. In most cases, these aerosols are fragments from common silicate and

carbonate rocks of the Earth's crust, however, they can also be of organic or soot origin. Soluble impurities originate by deposition from the atmosphere or by incorporation of bedrock material into the glacier's basal layers. Contrary to temperated glaciers, where a great part of the soluble impurities are washed out by percolating water, polar ice sheets retain soluble impurities for long time scales (Cuffey and Paterson 2010).

A simplified ion budget of the most significant anions and cations in the alpine and polar snow can be written as follows (Kreutz and Koffman 2013):

$$[Na^+] + [NH_4^+] + [K^+] + [H^+] + [Ca^{2+}] + [Mg^{2+}] = [Cl^-] + [NO_3^-] + [SO_4^{2-}]$$
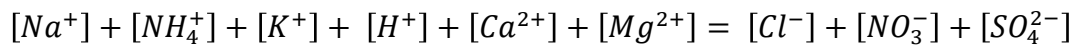
Following, major primary and secondary aerosols are introduced: sea salts, continental dust, black carbon, sulfur compounds and nitrogen compounds. The primary aerosols type describes particles as for example dust, sea salts, black carbon or microbes that are picked up by winds and thus become aerosols directly. And the latter type that includes sulfur and nitrogen compounds are aerosols that form in the atmosphere from gases (Cuffey and Paterson 2010, Legrand and Mayewski 1997).

Sea salts

Sea salts are one of the main origins for primary aerosols. They are mainly comprised of chloride (Cl^-) and sodium (Na^+) and some sulphate (SO_4^{2-}), potassium (K^+), calcium (Ca^{2+}) and magnesium (Mg^{2+}). Both Greenlandic and Antarctic ice core records show low sea salt impurity concentrations, such as Na^+, during warm stages and a gradual increase in concentration over the past glacial (Cuffey and Paterson 2010, Legrand and Mayewski 1997); more specifically, Na^+ concentrations decrease by a factor of five during warm Dansgaard-Oeschger events (Wolff et al. 2010). Further, the records show seasonal cycles in sea salts with winter maxima and summer minima (Legrand and Mayewski 1997). It is understood that these modulations and the seasonal variations result from changes in the sea ice cover combined with changes in atmospheric circulation. However, the theories disagree on the dominating processes transporting the sea salts onto the ice sheet. One line of argument postulates that sea salt fluxes are controlled by the wind speed and the amount of open water close to the drill site. While sea ice extends during winter and glacials, high increases in wind speed need to make up for the longer transport distances in order to match the measured concentrations. A second line of argument suggests that higher concentrations originate from a brine layer

with frost flowers forming on the top surface of the sea ice. Thereby, both brines and frost flowers are enhanced in sea salts compared to the concentration of ocean water. This perspective argues that higher concentrations of sea salt aerosols reflect sea ice extension; which is – at least for Antarctica – believed to be the most likely explanation of sodium records (Cuffey and Paterson 2010, Kreutz and Koffman 2013).

Continental dust

Other primary aerosols – dust – are microparticles picked up by winds on the continents and transported through the troposphere to the poles. Their typical size lies in the range of 0.1 μm to 2 μm and their composition reflects minerals found in their geographical origin. While most of these microparticles are insoluble silicate minerals, some are soluble carbonates like $CaCO_3$ and $CaSO_4$. Thus, calcium ions are also a proxy for wind-deposited dust. Via geochemical fingerprinting it was shown that the dust deposited on the Greenlandic ice sheet during the last glacial originates from central Asia, while the major dust source for Antarctica is Patagonia (Cuffey and Paterson 2010, Fischer et al. 2007, Wolff et al. 2010). As also seen with sea salts, dust records in ice cores of both hemispheres show dramatically higher concentrations in glacial climates and lower concentrations in interglacials. This pattern of increased dust concentrations by a factor of 20 and 10 in central Antarctica and central Greenland respectively, cannot only be produced by more efficient atmospheric transports but must also reflect stronger sources; it is suggested that the increase results from a combination of stronger winds, drier sources and longer transport times due to less precipitation and larger sources (Fischer et al. 2007). Furthermore, in the northern hemisphere a major component of the dust during a glacial is made up by $CaCO_3$, pointing to a different dust source, possibly exposed beds of former desert lakes. The carbonate minerals thus neutralize acids and leave the glacial ice alkaline (Cuffey and Paterson 2010). Calcium is deposited in Greenland in the northern hemisphere spring with mineral dust, while in Antarctica both a southern hemisphere summer peak for calcium from mineral dust and a winter peak for calcium from sea salts can be observed (Legrand and Mayewski 1997).

Black carbon

Black carbon or soot is released into the atmosphere in the process of burning fossil fuels, vegetation or other organic materials due to the incomplete combustion of these materials. Small amounts – on the level of a few nanograms per gram of ice – can be measured in Greenlandic firn. The addition of black carbon onto the ice triggers the albedo feedback, contributing to the warming of the atmosphere due to the higher absorption of solar energy by the black particles compared to the otherwise white ice and snow surface. It has been shown that black carbon concentrations have been peaking in the period from 1890 to 1950 with a tenfold increase in the concentrations by 1910 compared to concentrations before and after that time period. Therefore, the rise in concentration can be attributed to anthropogenic fossil fuel combustion (Cuffey and Paterson 2010).

Sulfur compounds

Important acids in the ice are sulfuric acid (H_2SO_4), resulting from the dissolution of sulfur dioxide (SO_2) in water droplets, and methane-sulfonic acid (MSA). Both MSA and SO_2 are products of atmospheric oxidation of dimethyl sulfide gas (DMS) that is produced by phytoplankton in the upper ocean. In addition to these biogenic sources of sulfur compounds, other non-anthropogenic contributions derive from sea salts and volcanic activity. On average, the contribution of volcanoes is small compared to biogenic sources. However, major volcanic eruptions, injecting hydrogen sulfide (H_2S) and sulfur dioxide gases that oxidize to sulfuric acid aerosols, as well as silicate microparticles into the stratosphere, lead to large acid spikes in the ice record for a few years following the eruption (see chapter 3). In addition to these natural sources, anthropogenic activities, especially coal burning, led to an increase in sulfuric acids accumulating in Greenlandic firn. However, this clear anthropogenic signature is not observed in Antarctica or Northwestern Canada (Cuffey and Paterson 2010).

Nitrogen compounds

Nitrogen oxide compounds are collectively referred to as NO_x. Nitrate (NO_3^-) – just as sulfuric acid described above – shows a similar increase due to anthropogenic fossil fuel use with industrial activities. In addition to this anthropogenic signal, sources for the baseline nitrate concentration in ice can be plentiful: bacterial emissions, biomass

burning, lightning, photochemical reactions and even, to a small extent, sea salts. The complexity from the mixed sources as well as a range of depositional and post-depositional processes hinder a conclusive interpretation of nitrate measurements in ice cores. Another important nitrogen compound is ammonium (NH_4^+), which is strongly linked to the biosphere; it derives from soil and biota emissions as well as biomass burning (Cuffey and Paterson 2010). In Greenland ice cores, ammonium impurities allow for the reconstruction of boreal forest fires (Kreutz and Koffman 2013). Also, concentrations exhibit a strong seasonal cycle with summer maxima due to vegetation growth (Legrand and Mayewski 1997).

2.3 Ice core research history and the EastGRIP project

Ice core research revolutionized our understanding of the climate of the Quaternary: The ice core archive opened a new portal to the past and successfully bridged the then persistent gap between climate records from tree rings and marine or lake sediments. The first deep ice cores from both Greenland and Antarctica were successfully retrieved and studied by the US Army Snow, Ice and Permafrost Research Establishment (SIPRE) from 1956 to 1959. The results encouraged the drilling of the first core to reach bedrock at Camp Century, Greenland, in 1966, followed by the drilling at Byrd Station, Antarctica, in 1968. The ice from Camp Century thereby provided the first direct evidence for a measurable, long-term record of the Earth's climate stored in the polar ice sheets. The pioneering idea of Willi Dansgaard to use oxygen isotope ratios as a proxy for past temperatures set the ground for a new discipline in geophysics. His initial work on the bedrock Camp Century core, after earlier oxygen isotope studies, thereby laid the groundwork for all subsequent ice core research (Langway 2008). Since then, multiple deep, intermediate and shallow ice cores have been drilled at both Greenland and Antarctica sites, as seen in figure 1. They span a wide range of different time scales. The ice retrieved from Greenland dates back to the last interglacial, the Eemian, while the Antarctic ice record dates back to around 800,000 years (Bradley 2015).
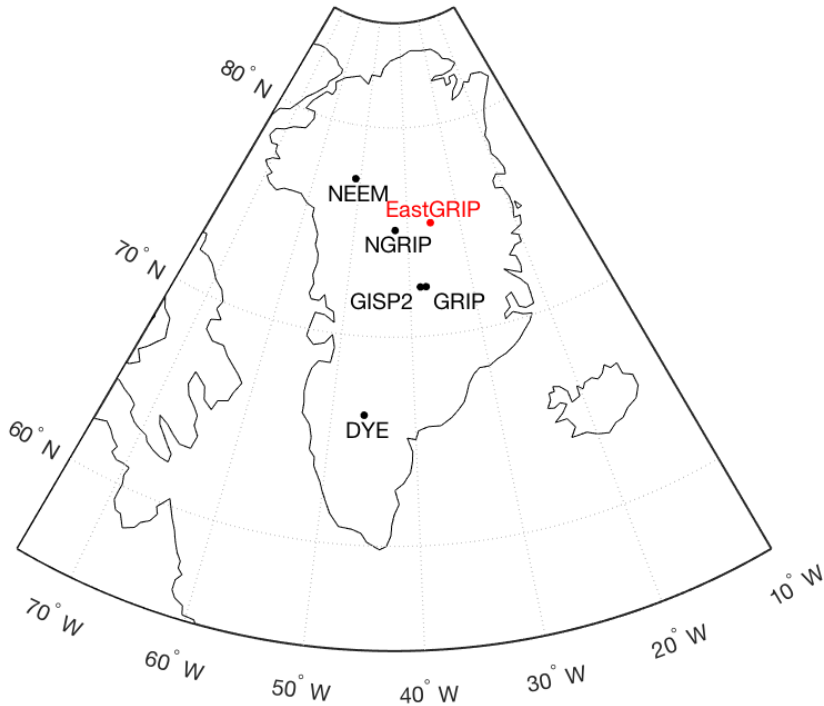
Figure 1: Drilling sites of several ice core drilling projects on the Greenland ice sheet.

A major challenge in ice core drilling projects constitutes the brittle ice zone. At depth, the increasing pressure from overlying ice masses on the trapped air bubbles causes the ice to fracture when exposed to the atmospheric pressure. Neff (2014) postulates that the mean brittle ice zone depth extends from 545±162 m to 1132±178 m below surface. As the air bubbles transform to clathrates with increasing pressure, the ice becomes more ductile (Neff 2014).

The brittle ice zone hampers ice core quality and subsequently paleoclimatic data. Many analysis techniques performed on ice cores depend on a low amount of fractures, as they constitute the risk of contaminants altering the paleoclimatological signal, as drilling fluid permeates fractures and even hairline cracks that emerge while drilling in the brittle ice zone. In CFA measurement systems, contaminations do not only impact the data of the contaminated ice core section, but further impact the measurement data of the subsequent ice, because it takes some time until the relatively high concentrations of contaminants are washed out of the sample lines and instruments. During the NEEM ice core CFA analysis, as an example, 27 instances of drill liquid contamination were identified in 175 m of ice from the brittle ice zone (Neff 2014).

Due to the high contamination and fragmented ice, there is an area of discontinued CFA data corresponding to the NEEM brittle ice zone (Schüpbach et al. 2018). In that instance, the NEEM brittle ice zone ranges from 609 m to 1281 m depth, corresponding to around 3 ky to 9 ky BP. Innovative techniques for drilling and strategies for the handling and transport of the ice aim at minimizing fractures of the ice in the brittle ice zone (Neff 2014). This has helped increase the quality of EastGRIP ice for CFA measurements. And as the brittle ice zone affects different ages in different ice cores, depending on snow accumulation rate and ice thickness, one objective of this study with EastGRIP data is to contribute to filling in the area of discontinued CFA data of the NEEM ice core.

The EastGRIP project drills through the Northeast Greenland Ice Stream (NEGIS) aiming at improving our understanding of ice stream dynamics and their contribution to sea level change (EastGRIP 2019). The first 905 m of the estimated 2550 m long ice core were measured in the CFA laboratory in Berne. The range from meter 350.35 to 904.75, corresponding to a time range spanning roughly from 3 ky to further than 7.6 ky before 2000 CE, was measured during the EastGRIP CFA campaign 2019 and will be used for the analysis of this study.

3. Acidity

Volcanic eruptions have a significant impact on the Earth's climate. High amounts of sulfur compounds ejected into the stratosphere during volcanic eruptions are the dominant cause for natural climate change on the annual and multi-decadal time scale and explain much of the climate variability in the pre-industrial area of the last millennium (IPCC 2013c). These climate responses to volcanic eruptions as well as how the acidity in ice cores as a proxy for volcanic eruptions can be measured as a theoretical background for the acidity method used in this study.

3.1 Volcanic eruptions and climate

Volcanic eruptions have a significant impact on the Earth's climate on different time scales as summarized in figure 2 and table 1. Volcanic eruptions inject gases like N_2, CO_2 and H_2O as well as microparticles into the atmosphere. Thereby, explosive and non-explosive volcanic eruptions differ in their atmospheric input: While explosive eruptions typically generate large quantities of lithic materials, they might not produce so much gas (Robock 2000).
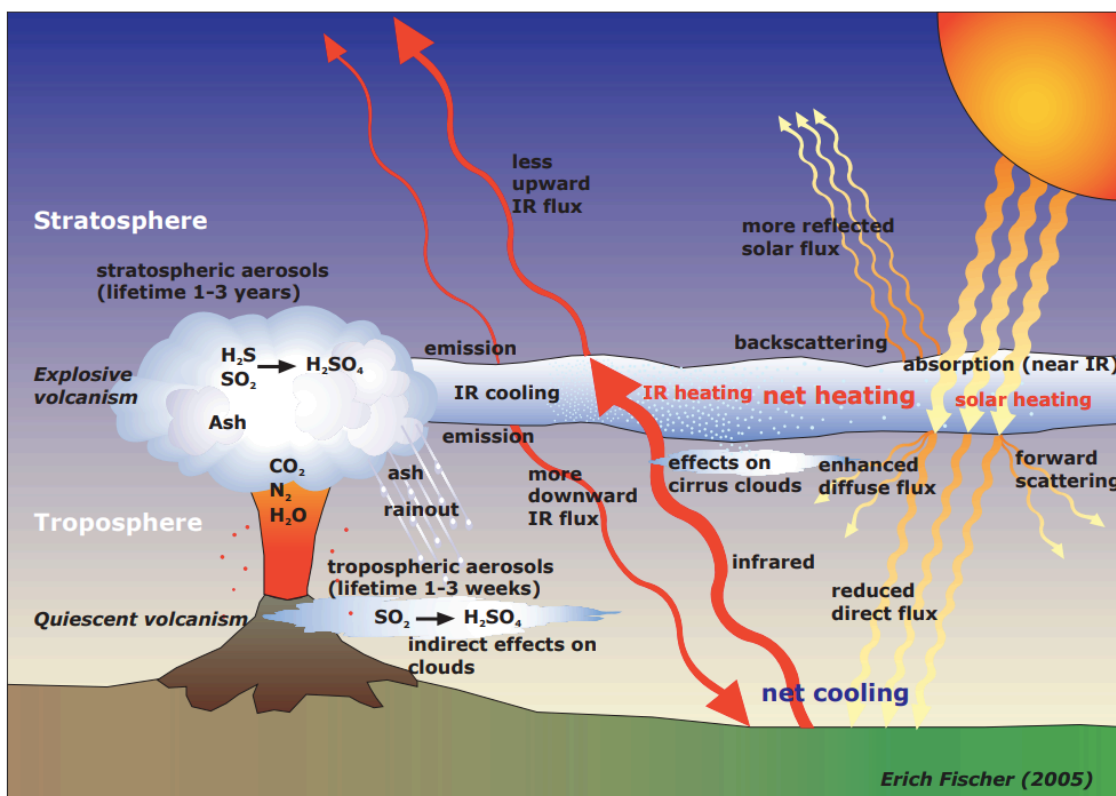
Figure 2: Schematic diagram of volcanic impacts on the Earth's radiative balance (Fischer 2006, p.9; adapted from Robock 2000).

The particles and chemicals of volcanic origin exhibit different atmospheric residence times, reflecting the different time scales of the volcanic impact on climate: First, CO_2 and N_2 generated by volcanic eruptions stay in the atmosphere for a long time. However, the additional input of these important greenhouse gases is negligible in comparison to their atmospheric concentration and does therefore not affect the greenhouse effect significantly. In contrast, siliceous ash particles of a size typically larger than 2 μm settle quickly after the eruption due to gravity. They are removed from the troposphere in a matter of minutes to weeks. In the stratosphere, small amounts can also stay up to a few months. The particles then significantly influence the diurnal cycle for a few days after an eruption, as they block ingoing as well as outgoing radiation. However, their impact on the global climate is short-lived and small (IPCC 2013c, Robock 2000).

The main volcanic impact on climate is linked to sulfur compounds in the form of mainly SO_2 and also H_2S. Within weeks, the sulfur compounds react in the atmosphere together with OH^- and H_2O to form H_2SO_4 aerosols that produce the dominant net cooling effect. The sulfate aerosol particles thereby scatter incoming solar radiation both back into space but also forward towards the Earth's surface. The net effect, however, is an increased planetary albedo, leading to a cooling of the Earth's surface temperature for one to three years. The maximum cooling is thereby found at the tropics and in midlatitude summer, as there is the most incoming radiative energy for the aerosols to block. The cooling, in turn, leads to a reduced hydrological cycle and subsequently to reduced tropical precipitation. In addition to the net cooling effect, the absorption of both ingoing and outgoing radiation also heats the stratosphere. As seen on the tropical eruption of Pinutoba 1991, this increase in temperature is thereby higher in the tropics than at the poles. The stronger temperature gradient between the equator and the poles changes the atmospheric circulation patterns, and in the Northern Hemisphere winter subsequently results in a winter warming effect of the Northern Hemisphere continents that exceeds the radiative cooling effect. Additionally, the sulfate aerosols serve as a surface for chemical reactions leading to the destruction of ozone in the stratosphere. As ozone depletion lowers the absorption of ultraviolet radiation, this effect reduces the heating in the stratosphere (Robock 2000).

These impacts on the climate system thereby depend on the geographic location of the volcanic eruption: While tropical volcanic eruptions can influence the global climate

system, as the aerosol cloud can disperse into both hemispheres, mid and high latitude volcanoes predominately affect the hemisphere they are on (Timmreck 2012).

Table 1: Impacts of large explosive volcanoes on weather and climate. Table modified from Robock (2000, p.202).

Effect	*Mechanism*	*Begin*	*Duration*
Reduced diurnal cycle	Blockage of shortwave and emission of longwave radiation	Immediately	1-4 days
Reduced tropical precipitation	Blockage of shortwave radiation, reduced evaporation	1-3 months	3-6 months
Summer cooling of NH tropics and subtropics	Blockage of shortwave radiation	1-3 months	1-2 years
Stratospheric warming	Stratospheric absorption of shortwave and longwave radiation	1-3 months	1-2 years
Winter warming of NH continents	Stratospheric absorption of shortwave and longwave radiation, dynamics	½ year	One or two winters
Global cooling	Blockage of shortwave radiation	Immediately	1-3 years
Global cooling from multiple eruptions	Blockage of shortwave radiation	Immediately	10-100 years
Ozone depletion, enhanced UV	Dilution, heterogeneous chemistry on aerosols	1 day	1-2 years

With the exceptions of extremely big volcanic eruptions, the atmospheric residence time of volcanic aerosols is generally limited to two or three years. Subsequently, the climatic impact of volcanoes is more on an annual than on a decadal or centennial time scale. However, Robock (2000) proposes that a longer time interval with multiple eruptions could lead to a multi-decadal global cooling effect. Conversely, a warming effect is produced through the adjustment of the climate system after a longer time period of active volcanism. Since the Pinatubo eruption, for example, there has been no major volcanic eruption with a significant influence on the global climate. Still, several smaller eruptions led to a net change in the energy balance of the climate system of -0.11 Wm^{-1} or -0.06 Wm^{-1} between 2008 and 2011 with reference to 1750 and 1999-2002 respectively (IPCC 2013c). This radiative forcing resulted in a global cooling effect of 0.4 K and a stratospheric warming of 2-3 K (Timmreck 2012).

The Pinatubo eruption in 1991 is the best documented volcanic eruption to date. Since the late 1970s global coverage of stratospheric aerosol has been possible due to several satellite platforms (IPCC 2013c). Since major volcanic eruptions affect the whole climate system, data on volcanic eruptions can be used extensively for the improvement of climate and Earth system models (Timmreck 2012). A deeper understanding of natural climate fluctuations caused by volcanism in the past improves the understanding of important radiative and dynamical processes and fosters understanding of the anthropogenic impact on the climate. This, in turn, is crucial for improving climate model projections for climate change in the future (Robock 2000).

3.2 Acidity in ice cores

In ice cores, indications for volcanic eruptions can be detected as ash particles or acid layers as a result of precipitated sulfur compounds. Compared to biogenic emissions, the contribution of volcanoes to sulfur on the ice sheet is small on average, but can be large for a few years following an eruption. While in most cases, the microparticles settle fast and are not transported and deposited on the ice sheet, the volcanic aerosols are widely dispersed and washed out by precipitation. In this process, volcanic eruptions are recorded as layers of acidity in the polar ice sheets (Cuffey and Paterson 2010).

These records of volcanic activity in the ice – sulfate, acidity or tephra layers – are extensively used to date and cross-date ice cores. Greenlandic ice cores can be dated by annual with high accuracy by layer counting up until around 60,000 years back in time. Volcanic eruptions recorded in the ice can thus be used to constrain the age-depth relationship of other ice cores if the same eruption is detected in the ice. In this manner, Greenlandic ice cores have been stratigraphically linked by volcanic markers. Antarctic ice cores are aligned similarly (Bradley 2015, Svensson et al. 2008, Parrenin et al. 2012, Vinther et al. 2006).

Chapters 2 and 3 so far allow to conclude that the main value of measuring acidity in ice cores is twofold: First, an absolute measurement of the acidity in the ice is crucial for obtaining the full ionic balance (see section 2.2). And second, the relative values of acidity in the ice can be used to interpret the volcanic activity at the time. Next to volcanic activity, however, acidity in ice cores provides information on other environmental factors, such as anthropogenic pollution and Arctic haze. Further, as outlined in section 2.2, acidity is influenced by the neutralizing effect of carbonate

mineral dust ($CaCO_3$) making the glacial ice more alkaline, products from marine biogenic emission such as methanosulfonic acid (MSA), and ammonium from soil and biota emissions and biomass burning (Cuffey and Paterson 2010). The pH, in turn, determines the solubility of many ions and influences chemical reactions in the polar ice. Thereby it has been proposed that pH is a major factor of the in situ production of CO_2 in Greenland ice cores (Kjær 2014).

3.3 Determination of acidity in snow and ice cores

Several detection methods with links to the acidity of snow and ice are available. They are applied either to the ice or the meltwater from the ice core. First, two fast, non-destructive methods applied on a flat ice surface are the Electrical Conductivity Measurements (ECM) and Dielectric Profiling (DEP). Even though they do not obtain an absolute measurement of H^+ in the ice, these methods are performed during ice core drilling campaigns in order to rapidly obtain a preliminary record of volcanic eruptions and subsequently a rough dating of the ice (Kjær 2014).

An *Electrical Conductivity Measurement*, developed by Hammer et al. (1980), is performed by moving two electrodes with a voltage difference of typically 1250 V between them along a clear-cut ice core surface. The measured electrical current between the two electrodes reflects almost only the strong acids in the ice core and thus provides clear indications of acid volcanic horizons (Hammer et al. 1980, Wolff 1997). While most anions only have a small effect on the ECM method performance, the method is influenced by calcium. Thus, the high amounts of dust impede ECM measurements on Greenlandic ice cores and induce uncertainties. Also, the ECM signal in firn has to be corrected for the lower density as the air between the ice grains significantly lowers the electric current (Kjær 2014).

Dielectric Profiling, was originally developed by Moore and Paren (1987) with several optimizations undertaken later on. The method measures the conductivity and capacitance of the ice at different frequencies of up to 300 kHz by applying two electrodes on the ice core and sending an alternating electrical current through the ice (Wolff 1997). Contrary to ECM, calcium is not expected to influence the DEP method. DEP is mainly affected by H^+ in ice, with significantly smaller effect of sea salts such as Cl^- or Na^+ on the signal. Similar to ECM, however, measurements of firn need to be corrected for the lower density (Kjær 2014).

Second, a set of acidity detection methods detects acidity in the meltwater from the ice core. By design, these are thus destructive and more labor intensive but eliminate the density problem. On the other hand, the measurements on the melted sample are influenced by CO_2 both contained in the ice as well as well as in the ambient air with an unsealed measurement system (Kjær 2014). They include direct measurement methods such as titration of discrete samples as in the method by Legrand et al. (1982), or the modified titration method avoiding the effect of ambient CO_2 on the meltwater by Pasteris et al. (2012). Titration describes the process of adding a standard solution of known concentration to the solution to be measured until an equivalence point is reached where the amount of OH^- added is equal to the original H^+ concentration in the solution or vice versa. The equivalence point is then determined either by the change of color of an added indicator or by measuring the pH with an electrode (Chemistry LibreTexts 2019b). Further, indirect methods that determine the H^+ from the ionic balance (Kjær 2014, Kreutz and Koffman 2013, Legrand and Mayewski 1997), or meltwater electrolytic conductivity measurement (MWEC) exist.

As described in section 4.1, MWEC is a standard part of a continuous flow analysis system (CFA), reflecting all the major ions in the meltwater. Thus in Greenlandic ice cores the signal is mainly governed by dust with Ca^{2+} being the most predominant ion whereas for Antarctic ice cores the signal is highly determined by sea salts with Cl^- and Na^+ being the dominant ions. Also, higher levels of SO_2 from volcanic eruptions increase the conductivity of the meltwater, thus the MWEC signal also serves as an indicator for volcanic eruptions (Röthlisberger et al. 2000). The method offers high reliability and temporal resolution. However, similar to ECM and DEP, as MWEC does not uniquely measure H^+ concentrations, small peaks of acidity can be overridden by other ions measured in the ice. Still, they give indications of volcanic activity (Kjær 2014).

Kjær (2014) concludes that all the acidity methods presented above have shortcomings and are not reliable. To this end, Kjær et al. (2016) developed a continuous optical dye acidity method that is used in this study and is subsequently explained in section 4.2.

4. Methods

This chapter outlines the methodological design of this thesis. The first four sections introduce the continuous flow analysis and its typical components (4.1), the optical dye method for acidity detection used in this study (4.2), the theoretical background for the calibration of the acidity instrument (4.3) as well as quantitative quality criteria for detection techniques that serve as a guideline for the data analysis of this study (4.4). On the basis of that, the subsequent three sections describe the methodological procedure of the analyses performed in this study. These include a dye test aiming at optimizing the concentrations of the two pH-indicator dyes in the reagent (4.5), the evaluation of the method performance of the optimized Berne acidity setup (4.6) and the evaluation of volcanic indications in the EastGRIP CFA data (4.7).

4.1 Continuous flow analysis (CFA) system

Continuous flow analysis is a well-established measurement technique for the analysis of the impurity content of ice cores. As its name indicates, in a CFA system an ice core is continuously melted with the meltwater being distributed among different measurement techniques (Kaufmann et al. 2008). Over Ion Chromatography, as a standard measurement technique measuring both anion and cation concentrations of the sample, CFA offers a higher temporal resolution, less contamination as a result of reduced handling of the core while minimizing the time consumption used to do the measurements. On the basis of the pioneering work of Sigg et al. (1994), several CFA systems have been developed. In this section, the CFA system in Berne and its key components are described, as used in this project for the measurement of the EastGRIP ice core during the measurement campaign 2019.

The ice core pieces measured in the CFA analysis, so-called bags, have a square cross section of approximately 3.5 cm x 3.5 cm at a length of around 55 cm. The pieces are vertically placed above a melting device in a cooled environment of around –20 °C. Figure 3 shows a schematic of the CFA system in Berne. On the *melter head* the ice is continuously melted at a constant melting rate that depends on the density of the firn or ice that is melted. Thereby the melter head provides a non-reactive surface and its design splits the meltwater into a clear inner part used for the subsequent analysis techniques and a possibly contaminated outer part that goes to waste (Kaufmann et al. 2008, Kjær 2014).

A melting speed detector, the so-called *encoder*, consists of a wire attached to a weight that lies on top of the ice core to be melted and an optical encoder. The encoder measures the movement reflecting the melting speed of the ice core in the CFA system in counts per second. From this data the melting speed for the entire core can be calculated and subsequently translated into a depth scale while correcting for missing pieces of the ice, as for example removed internal breaks, or end cuts of the ice core (Röthlisberger et al. 2000).

Peristaltic pumps pump the inner part of the sample into the heated working room and through a *debubbler* in order to prevent air from getting into the analytical modules (Kaufmann et al. 2008). Whereas the Berne system uses an open debubbler, a sealed debubbler used in the CFA system in Copenhagen minimizes the mixing volume of the sample. A debubbler also allows the separation and subsequent separate analysis of the gas that was trapped in the ice (Bigler et al. 2011). Furthermore, it offers an advantage for pH detection: The sample does not get in contact with the ambient air, thus eliminating possible effects of ambient CO_2 on the detection method. After the removal of gas from the meltwater, the sample is split into different detection lines where the sample is analyzed for multiple environmental and climate proxies.
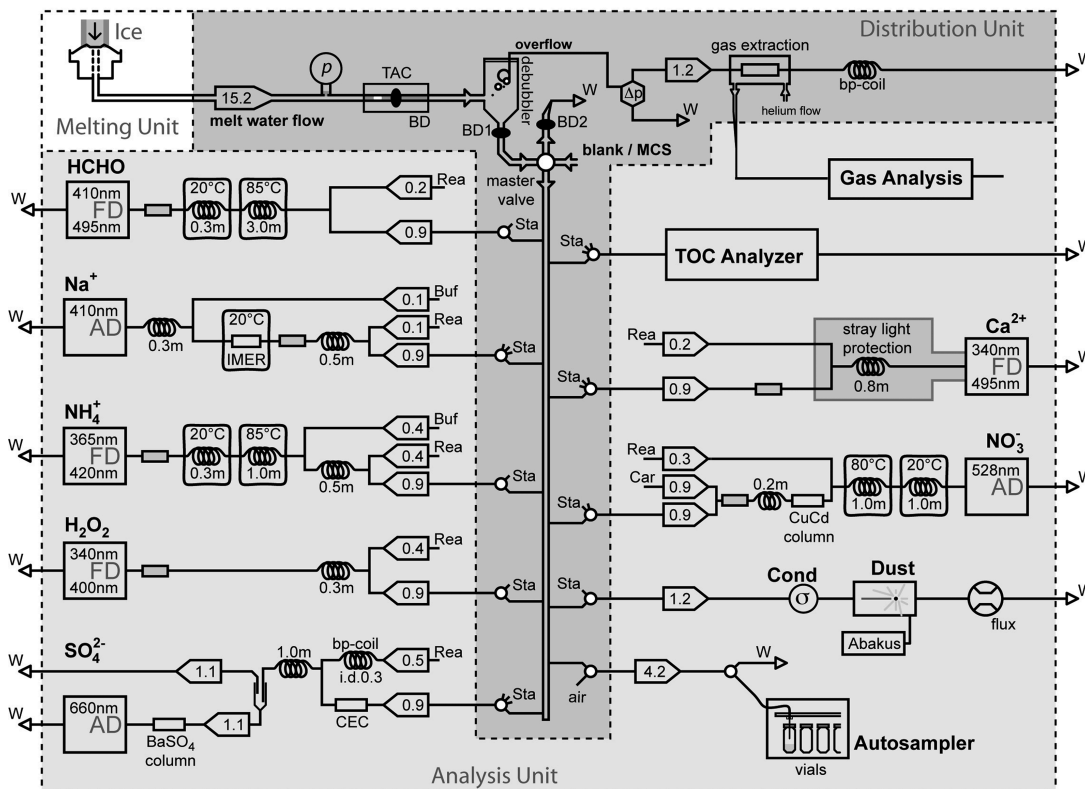
Figure 3: Schematic of the CFA setup in Berne, Switzerland (Kaufmann et al. 2008, p.8045).

Two measurements that are typically part of a CFA system are dust and MWEC. The *MWEC* measurement technique is described in section 3.3. Both the detection of dust and MWEC are performed on the sample alone, without the addition of a buffer or reagent (Kaufmann et al. 2008) Thus the sample can be used for other detection techniques afterwards. In this manner a conductivity cell can be placed in front of multiple other detection instruments. While offering a very high time resolution, the MWEC signal can be used in this way to synchronize the different detection signal in the data processing (Kjær 2014).

Insoluble *dust* particles are determined with an Abakus laser sensor. The particle detector uses a laser to detect particles flowing through its detection cell. The channel of the detection is so narrow that in theory only one dust particle can flow through it at a time, resulting in a signal of particle counts per second. In order to translate the signal to counts per mL, a flow meter exactly determining the flow is installed in front of or after the Abakus. In addition, a discrete and more precise instrument measuring particles as well as their size distribution – called Coulter Counter – is often coupled to the Abakus system in order to obtain a size distribution of the insoluble particles detected (Kjær 2014).

Further, various concentrations of ions of interest are detected by fluorescence and absorption detection methods. In figure 4 an example for an absorption and a fluorescence measurement, standard series and the corresponding calibrations are shown. All *absorption techniques* detect the ion of interest based on its absorption of light. The fundamental functionality of absorption techniques is outlined in section 4.3. On the other hand, *fluorescence techniques* are based on the molecules of interest being excited to a higher energy state through the absorption of incoming photons. With time, the molecule decays and emits a photon with different energy than the originally absorbed photon. The emitted photon can thus be detected at a different wavelength than what was used to excite the molecule. An optical filter is often used to ensure that only the emitted light is measured. For both the absorption and fluorescence methods, standards of known concentrations are measured in order to produce a linear calibration between the concentration of the molecule of interest and the detected signal. In section 4.3, only the calibration method used for absorption method is described, as this is the calibration performed on the EastGRIP CFA acidity data.
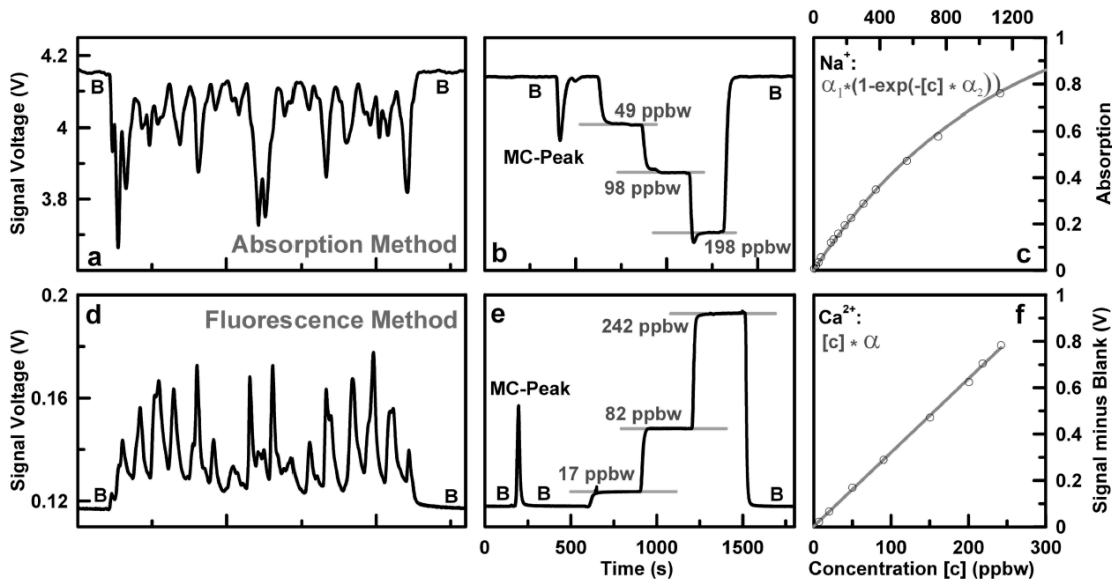
Figure 4: An example of a typical sample signal (a,d), standard series (b,e) and the corresponding calibration curves (c,f) for both an absorption (Na^+, top panel) and fluorescence (Ca^{2+}, bottom panel) method in the Berne CFA system.

Next to these standard components of a CFA system, an optical dye method for the detection of acidity is described in section 4.2. This method was originally developed by Kjær et al. (2016) and an optimized setup was built into the Berne CFA system, as seen in figure 3, for the EastGRIP measurement campaign 2019.

4.2 Optical dye method for acidity: Original and restructured method setup

The continuous detection method for acidity in ice cores used in this project was developed by Kjær et al. (2016). The method used is an optical method, spectroscopically detecting the color change of two pH-indicator dyes, bromophenol blue and chlorophenol red. Bromophenol blue changes its color from yellow at pH 3.0 to blue or violet at pH 4.6 and chlorophenol red changes from yellow at pH 4.8 to violet at 6.7. Thereby, this range represents the pH measured in polar ice cores of pH 4.49 to pH 6. The dye concentration used by Kjær et al. (2016) amounts to 0.05 mg/mL with a 1:1 mass ratio of the two indicator dyes, as this ratio was found to yield the largest color change within the range relevant for polar ice cores. The dyes are mixed with Brij L23 that enables air bubbles to flow more easily through the absorption cell and diluted with MilliQ (ultra pure) water; the recipe with the respective masses can be found in table 2.

Table 2: Recipe for dye reagent used in Kjær et al. (2016) resulting in a dye concentration of 0.05 mg/mL.

Substance	Mass / Volume
Bromophenol blue	0.025 g
Chlorophenol red	0.025g
Brij L23 (30 % w/v)	100 µL
MilliQ water	500 mL

The set up of the method is schematically represented in figure 5. The acidity method line is part of the CFA set up described in chapter 4.1 with the ice being melted on the melter head (MH). The sample is pumped through an injection valve (IV) and a selection valve (SV) that allows the switch between blanks (Bl), standards (St) and sample (Sa). The debubbler (D) separates the gaseous components naturally occurring in ice and firn. The gas (GE) can then be separately analyzed. After that, the sample is split into different measurement lines (DO); only the acidity line is shown in more detail in figure 5: The sample (Sa) is mixed with the dye reagent and passed through a mixing column of 1 m length to improve the mixing of the sample with the added reagent. In order to control any temperature effects and theoretically minimize the CO_2 content in the sample, a heat bath keeps the sample at a stable temperature of 65 °C. In theory, the CO_2 uptake of the water is temperature dependent, however, Kjær et al. (2016) showed that the temperature of the heat bath has no significant effect on the measurements. This thus suggests that the optical dye method is not influenced by ambient CO_2 concentrations, at least not to a measurable extent. After the mixing, the sample is led through an accurel (Ac) that has an air-permeable membrane but is impassable to water. The accurel thus removes any newly formed air bubbles produced in the heating process. Then the sample passes through a 2 cm long absorption cell. If there are still air bubbles in the sample line that were not removed by the accurel membrane, the Brij L23 added to the dye reagent facilitates the removal of air bubbles from the absorption cell. In the absorption cell, the light intensity (A) is measured with a spectrometer (Ocean Optics USB 2000) at two wavelengths, 450 nm and 589 nm, which show an optimum response in the color change measured as ($-\log_{10}(I/I0)$). As will be discussed in section 5.1, the spectrometer has noise introducing properties. Further, a white light-emitting diode (LED) is used as the light source for measuring the light intensity. After the measurement, the sample goes to waste (W). The arrow boxes represent peristaltic

pumps, with the respective flow rate in mL/min. Kjær et al. (2016) detect that the reagent mixture works well with a flow of 0.15 mL/min for the reagent and 0.9 mL/min for the sample.
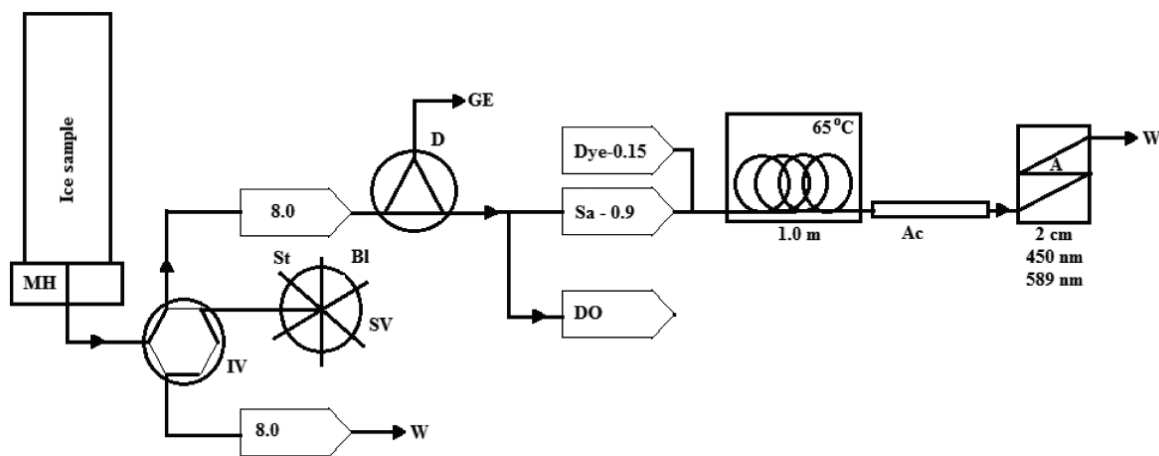
Figure 5: Schematic illustration of the set up of a continuous flow method for acidity, developed by Kjær et al. (2016, p.10486).

The optical dye acidity method described here exhibits several sensitivities. Air bubbles flowing through or getting stuck in the absorption cell disrupt the acidity signal: The air bubble blocks some of the emitted light by the LED, thus lowering the detected signal. Further, Kjær et al. (2016) argue that the technique is sensitive to the mixing ratio of the sample and the dye reagent. Differential wearing of the tubing leads to flow changes over time, which, in turn, influences the mixing ratio. In line with this, Kjær et al. (2016) observe a linear drift caused by the ageing of the tubing. An additional drift over time stems from the ageing of the bromophenol blue dye, however, mainly at the 450 nm wavelength. Moreover, during the Antarctic RICE measurement of glacial ice, an influence of dust on acidity measurements was observed. Theoretically, the influence of dust is twofold: First, soluble $CaCO_3$ that constitutes a major component of dust during a glacial mainly in the northern hemisphere, neutralizes acids and thus leaves the glacial ice more alkaline. Second, similar to air bubbles, insoluble dust particles flowing through the light path might block some of the light and subsequently lower the detected acidity signal. As the Antarctic RICE core does not contain high amounts of dust, it can be hypothesized that the influence might rather be linked to the dust size (personal communication, Helle Astrid Kjær, 27 May 2019). This short overview of different factors influencing the acidity detection is by no means exhaustive but aims at providing an insight into the complexity of the interconnections influencing the performance of the technique.

24

With the aim of a further optimization of the method, the instrument setup used in the EastGRIP measurement campaign in 2019 was restructured. Table 3 compares the new optimized setup and the original setup developed by Kjær et al. (2016) described above. Instead of a white LED, the changed instrument setup uses an LED (Roithner Lasertechnik) that emits a band of yellow light with a peak wavelength of 590 nm. For the detection, a photosensor module is used (H9306-02, Hamamatsu) with a spectral response of 185 nm to 900 nm together with an optical band-pass filter (Edmund Optics, bandwidth 10 nm) in the spectrum of 589 nm. The combination of the wavelength-specific LED and the filter used enables the detection at the peak wavelength of 589 nm for the acidity method. As both the specific LED as well as the filter lower the light intensity, a photomultiplier (as part of the photosensor module) is needed in this setup to achieve a detectable signal. The signal is detected as an electric potential difference, voltage (V). As in Kjær et al.'s (2016) setup, a mixing coil of 1 m length was used. A basic test with a 0.5 m and 1 m long mixing coil, further described in section 4.5, did not show any differences in sensitivity. In order to ensure complete mixing, a 1 m length was opted for. The method does not use a heat bath of any sort. However, the module that holds the acidity method within the Berne CFA is temperature-stabilized at 22 °C. As described above, Kjær et al. (2016) tested the dependence of the method on temperature, with temperatures ranging from 25 °C to 75 °C without finding a significant effect. As both the specific LED and the photosensor module are not temperature dependent, it can thus be assumed that the lower temperature of 22 °C in this setup should not influence the method to an observable extent. Furthermore, as the whole acidity instrument is mounted into the temperature-regulated box, baseline drift and signal noise induced by changes in temperature are theoretically minimized (Kaufmann et al. 2008, Kjær et al. 2016). Hereafter, the restructured acidity setup used in the EastGRIP measurement campaign 2019 is called the Berne setup.

In conclusion, the method used in Berne in 2019 differs from the originally developed setup described in Kjær et al. (2016) in the main points summarized in table 3: Instead of a white LED, the 2019 optimized setup uses a LED with a specific wavelength and an optical bypass filter, enabling the detection at the peak wavelength of 589 nm for the acidity method. Further, the Berne setup uses a photosensor module with a photomultiplier coupled with a transmitter in contrast to the spectrometer used by

Kjær et al. (2016). Next, the calibration of the instrument and the conversion of the detected signal to measures of concentration are introduced.

Table 3: Comparison of the Copenhagen setup as described by Kjær et al. (2016) and the adjusted Berne setup used during the EastGRIP CFA measurement campaign 2019.

	Copenhagen setup: Kjær et al. (2016)	*Berne setup*
Light source	White LED (6000 mcd, 18° dispersion, FIA Lab Inc. USA)	LED with peak wavelength of 590 nm (Roithner Lasertechnik) with custom current driver
Optical filter	none	Optical band-pass filter (Edmund Optics, wavelength 589 nm, bandwidth 10 nm)
Detection	Spectrometer (Ocean Optics USB 2000)	Photosensor module (H9306-02, Hamamatsu) with a spectral response of 185-900 nm and a photomultiplier with a 1 V/µA conversion factor

4.3 Standard series and calibration

In order to calibrate the instrument, standard solutions of known concentration are run through the CFA system. Standard runs are undertaken multiple times a day; this minimizes calibration uncertainties due to changing measurement conditions and facilitates the correction of shifting baselines. The standard solution of both the alkaline (NaOH) and acid (HCl) concentrations used in the EastGRIP measurement campaign are presented in table 4. Note that the concentration of both the NaOH and HCl solutions were halved in the second week of the measurement campaign (28 Jan 2019), in order to better represent the detected acidity range. The uncertainty calculated for the standard concentrations shown in table 4 results from the random variability in the volume of both the pipetted chemistry as well as the MilliQ water used to prepare the standard solutions. Thereby, a volume error of 0.8 % was assumed for the pipetting as well as a variability of ±0.1 mL for each 20 mL of MilliQ water.

Table 4: Standard recipe and concentrations with the uncertainty range of NaOH and HCl standards used during the EastGRIP measurement campaign 2019. On January 28, starting with the standard data file 190128-008.EGRIP.sta.dat, the concentration of all standard solutions was halved (Email communication, Camilla Marie Jensen, 27 March 2019).

Acidity standard solutions: HCl and NaOH			μL	mL	μM
Stock solution					100,000.00
Before 28 Jan 2019	1st Dilution		600	60	990.10
	2nd Dilution	High	1200	60	19.41 ± 0.50
		Low	600	60	9.80 ± 0.25
After 28 Jan 2019	1st Dilution		200	20	990.10
	2nd Dilution	High	600	60	9.80 ± 0.25
		Low	300	60	4.93 ± 0.13

The acidity measurement technique does not directly measure the concentration of the analyte interest in the meltwater. As discussed above in section 4.2, the signal in the Copenhagen setup is measured as light intensity, as counts of photons per second, whereas in the Berne setup, the signal is transformed to voltage. Subsequently, the signal has to be converted into measures of concentration in order to analyze the data.

Even though the original setup of the acidity method corresponds with absorbance methods, the presented method can neither be classified as a fluorescence nor an absorbance method. Instead, as described above, it is an optical dye method. However, in line with the methodological process of Kjær et al. (2016), in this study the acidity data was calibrated by absorption.

Absorption methods measure the concentration of the species of interest by their absorption of light. Light of intensity I_0 is introduced into the waveguide and the intensity I_1 coming out on the other end is measured. If some of the light was absorbed by the analyte led through the absorption cell, then $I_1 < I_0$. Absorbance is thus defined by the incoming and transmitted light intensity as follows:

$$A = -log_{10}\left(\frac{I_1}{I_0}\right)$$

The absorbance is based on two assumptions: First, absorbance (A) is directly proportional to the concentration (c) of the analyte in the sample. This linear relationship, however, does not apply to very high concentrations (>0.01 M). And second, the absorbance is directly proportional to the length of the waveguide (l). Note that the latter means that an increase in the length of the waveguide leads to a better limit of detection. These two relations can be written as the Beer-Lambert Law, by also introducing a constant for the wavelength dependent molar absorptivity to base 10 in $M^{-1}cm^{-1}$:

$$A = \varepsilon \cdot l \cdot c = -log_{10}\left(\frac{I_1}{I_0}\right)$$

From the standard solution we can derive $\varepsilon \cdot l$, while the absorbance can be determined by subtracting the baseline MilliQ signal from the sample signal. A linear calibration curve is fitted through the standard concentrations and forced through zero, as per definition the concentration is zero with zero absorbance. An example of a standard run and the resulting calibration curve for acidity is shown in figure 6. In the next step, the concentrations of the raw ice core measurements can be calculated based on the calibration coefficients (Chemistry LibreTexts 2019a, Kaufmann et al. 2008). Kjær et al. (2016) produced a separate linear fit through the NaOH and HCl standards respectively. They argue that the difference in the relationship between absorption and concentration is likely a result of a different strength in the response of the dyes when it comes to more and less acidic standards. Unlike Kjær et al. (2016), this study produced one calibration curve with both the NaOH and HCl standards.
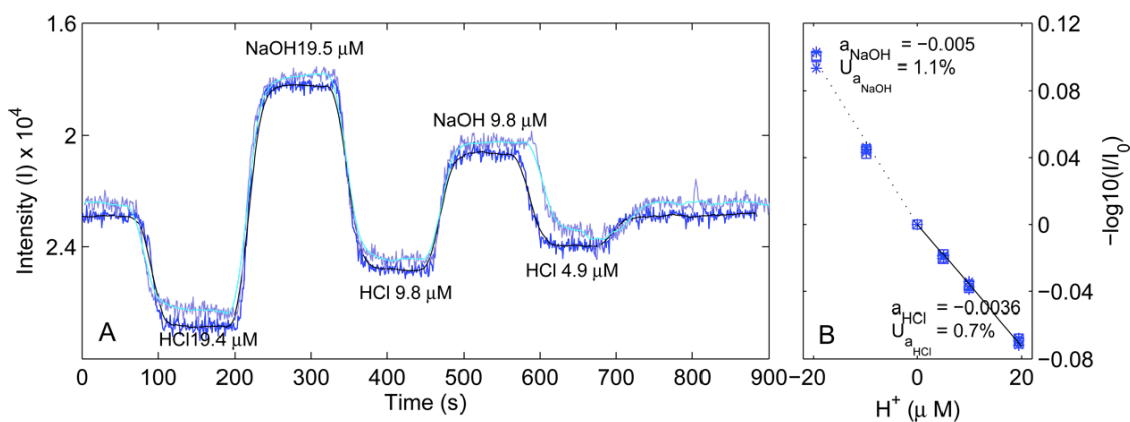
Figure 6: Example of two standard runs (A) measured at 589 nm with standard concentrations of 19.4 μM HCl, 19.5 μM NaOH, 9.8 μM HCl, 9.8 μM NaOH and 4.9 μM HCl. Panel B shows the standard calibration. On the x-axis the NaOH concentrations are referred to as negative H$^+$. A separate linear curve is fitted through the NaOH (dotted) and HCl (line) standard concentrations (Kjær et al. 2016, p.10488).

4.4 Quality criteria for the evaluation of a detection method

Bigler (2000) proposes six quality criteria of quantitative analysis for the evaluation of a detection method: precision, measurement accuracy divided into statistical and systematic errors, sensitivity, detection limit, operational area and selectivity. Additionally, the temporal resolution and the signal to noise ratio are of great interest when evaluating a detection method. The quality criteria described in this section serve as a guideline for the methodological backbone of the data analysis – the assessment of the restructured acidity setup and the dye test with regards to the method optimization as well as the method performance during the EastGRIP measurement campaign 2019.

The *signal to noise ratio* is of high importance when assessing a method or instrument as the noise is often constant and independent of the signal strength. The lower the signal, the higher is the impact of the noise on the measurement error. Thus, in maximizing the signal to noise ratio by either reducing the noise or elevating the signal, the quality measures of a certain method or instrument can be improved (Bigler 2000).

Precision is a measure for the reproducibility of a method. It is defined as the degree of closeness of the results produced in the same way, by asking whether the method is able to produce the same results over and over again. It can be assessed with the standard deviation (Bigler 2000).

Measurement *accuracy*, on the other hand, is the ability of the method to measure a value that is exact or close to the actual value. It is defined by the relative and absolute error. Statistical errors that can be handled using statistical methods can be distinguished from systematic errors. The latter are both more difficult to detect and to remove from the data. An important systematic error in a detection method is a drift that could be induced by temperature changes or the tubing. Further, standard concentrations are prone to systematic errors. Also, different chemical and physical factors can lead to a systematic error, such as unstable standards and reagents or slow chemical reactions (Bigler 2000).

The *sensitivity* of the instrument is defined as its ability to detect small variations in the concentration of the analyte and is controlled by two factors: the slope of the calibration curve and the precision of the instrument. As described above, the precision can be assessed with the standard deviation. Both factors are equally influential, meaning that if two methods exhibit the same precision, the one with the steeper slope is the more

sensitive one. Conversely, if two methods have the same slope of the calibration curve, the one with the lower standard deviation is the more sensitive one (Bigler 2000).

Another quality criterion is the *detection limit*, which describes the minimal concentration of an analyte that can still be detected with a known statistical certainty. The signal can only be reliably detected if it is a factor c greater than the variability of the blank signal, which is given by the standard deviation of the baseline signal. Often, the factor c is chosen at three, meaning that the lowest detectable signal is greater/smaller than the baseline signal plus/minus three times its standard deviation (Bigler 2000).

The *operational area* (ger.: Arbeitsbereich) is defined as the viable area for quantitative detection, ranging from the lowest concentration at which the analyte can quantitatively be recorded to the concentration at which the calibration curve moves out of the linear range. Equivalent to the detection limit, the lower limit of the operational area is often quantified as the baseline signal plus/minus ten times its standard deviation (Bigler 2000).

The *selectivitiy* of a detection method quantifies the degree to which it is influenced by other species, as no method is totally unaffected by other species than the analyte of interest occurring in the sample. The quantification with selectivity coefficients reflecting the interference of other species builds on the Beer-Lambert Law (see section 4.3) for a multicomponent system (Bigler 2000).

Lastly, the *temporal resolution* is an important quality measure for continuous ice core measurements. The temporal resolution of the detection system is measured with the response time, defined as the time required for the signal to go from 10 % to 90 % of the peak response after switching from baseline to standard solution. Thus, the steeper the slope between the two plateaus, the shorter the response time (Bigler 2000, Kaufmann et al. 2008).

This short excursion into quality criteria in the quantitative data analysis serves as the foundation for the methodology of the evaluation of the acidity detection method in sections 4.5 and 4.6. Even though not all quality criteria were used in this study, it is still important to note their interrelatedness.

4.5 Dye tests: method optimization

In order to investigate the performance of the slightly changed acidity method setup and possible optimizations, a set of tests was performed in December 2018 in Berne, Switzerland. In these tests, the focus lay on investigating and optimizing the dye concentration of the reagent while all other variables were kept constant. While Kjær et al. (2016) already tested different dye concentrations; test included changing both the dye concentration and the ratio of the two indicator dyes at the same time. Thereby, they found an optimal performance of the acidity method with a dye reagent of a concentration of 0.05 mg/mL. To complement their obtained results, this dye test was specifically set up to investigate the impact of the dye reagent concentration on the method performance. This sections outlines the dye test executed and the methodological process of the data analysis.

For the test, a strong dilution of the dye reagent was prepared with 0.38 g bromophenol blue, 0.38 g chlorophenol red, 2 mL 5 % Brij L23 diluted to 750 mL MilliQ water. From this stock solution, eleven dilutions were prepared that cover a range of approximately 0.01 mg/mL to 0.1 mg/mL, which offer a range of weaker and stronger reagents than the concentration determined by Kjær et al. (2016) (see table 5).

The order of the different reagents was randomized in order to minimize systematic effects from the previously tested concentrations. Also, MilliQ water was run in between each of the reagents. However, effects of a strong concentration run just before a weaker one, thereby slightly strengthening the latter's concentration, cannot be ruled out. The test run for each of the eleven reagents consisted of a standard series with the following concentrations: NaOH 9.80 µM, HCl 19.41 µM and NaOH 19.41 µM. In cases with low quality of the test run such as air bubbles in the system, as seen by eye, the respective reagent was rerun. The entire test however, was executed only once. In order to improve the reliability of the results it would have been beneficial to run all reagents twice. Due to time limitations, though, this was not possible.

Table 5: Set up of the dye test for acidity method optimization

Order	mL of stock reagent to 40 mL MilliQ water	Dye concentration [mg/mL]
1	5	0.0561
2	1	0.0123
3	9	0.0928
4	3	0.0353
5	7	0.0753
6	4	0.0459
7	6	0.0659
8	11	0.1090
9	8	0.0842
10	10	0.1011
11	2	0.0241

As the first step of the data analysis, a linear calibration was established, as outlined in section 4.2. On the basis of that, the response time, the baseline signal as well as the slope of the linear calibration curve were investigated and thus served as quality criteria for the analysis of the method performance with changing dye concentrations. Standard runs with low data quality, such as strong drift, many air bubbles in the system, or else, were discarded. As in these instances the standard solutions were run a second time, it was ensured that there is test data of every dye reagent concentration tested.

In addition to the dye test, the effect of the length of the mixing coil on the instrument's sensitivity was tested. An assessment by eye led to the conclusion that the length of the mixing coil has no effect on the temporal resolution measured by the response time of the method. However, the data was not straightforward as multiple variables were changed at the same time and as there was a lot of drift. Thus, this experimental data was not further analyzed.

Further, an evaluation of the restructured acidity method setup, comparing two standard runs from the method developed by Kjær et al. (2016) and the optimized Berne setup,

complements the analysis of the acidity method optimization. The evaluation of the restructured method setup is presented in section 5.1 and the results from the dye test are presented in section 5.2.

4.6 Method performance analysis during EastGRIP campaign 2019

Further, this project investigates the method performance of the optimized Berne acidity setup based on the standard data over the six and a half weeks of the EastGRIP measurement campaign 2019. As introduced in section 4.3, the acidity detection technique is calibrated by running standard series multiple times a day. During the EastGRIP measurement campaign 2019, standards were run before the first and after the last run of the day, as well as in between all other runs. This results in a minimum of five standard runs with four measurement runs a day. Each run is equivalent to approximately 2 m to 3 m of ice being melted. The recipe of the standard solutions and their respective concentrations can be seen in table 4 (section 4.3). In case the standard run data was of low quality, such as when a lot of air bubbles were in the system, the calibration run was repeated. Before every measurement run, a piece of MilliQ ice of approximately 4.5 cm is melted. This makes the transition between the baseline signal of MilliQ water and sample clearly distinguishable.

The reagent used in the EastGRIP measurement campaign 2019 was of a concentration of 0.05 mg/mL. Before the start and towards the end of the measurement, a stock reagent was prepared (see table 6). Every week, a reagent was prepared by diluting 90 ml of the stock dilution to 750 ml MilliQ water. It can be assumed that this induced an ageing effect on the acidity detection method. It has to be noted that on one occasion, towards the end of the campaign (04 Mar 2019) the reagent used was prepared with a little less stock solution (no exact values available), lowering the concentration compared to the other weeks.

Table 6: Recipe and concentrations of stock reagent and the reagent used in the EastGRIP measurement campaign 2019.

	Recipe	Dye concentration [mg/mL]
Stock solution	0.35 g bromophenol blue 0.35 g chlorophenol red 2 mL 5 % Brij L23 750 mL MilliQ water	0.465
Reagent	90 mL stock reagent 750 mL MilliQ water	0.0498

Equivalent to the dye test data analysis, the first step of the quantitative data analysis consisted of descriptively assessing the data and the calibration. In the case of poor data quality, individual exceptions for the calibration computation were made in the software. In order to ensure measurement accuracy, it was assessed whether producing the calibration manually induced a systematic error, leading to different calibration coefficients than when done automatically. If the data quality did not allow a calibration to be performed, as for example due to air bubbles in the system or missing data, the data file was discarded. Further, data files where the slope or the intercept of the calibration curve exceeded two standard deviations were also discarded. For outliers of this scale it can be assumed, that the standard concentrations were off.

As also discussed in chapter 5, the acidity method showed a drift of the baseline. A few standard data sets showed substantial drift. Due to time constraints, the standard data was not corrected for the linear drift. However, the absorption calculation accounted for a sloping baseline. In order to correct the systematic error induced by drift (Bigler 2000), and ensuring higher method accuracy, the data would need to be detrended.

The analysis of the standard data of the measurement campaign first of all assesses different calibration options, such as the difference of including both NaOH and HCl standards compared to including only NaOH. The assessment of the method performance then focuses on the calibration coefficients over time, specifically on the slope of the calibration curve as a measure for the sensitivity of the acidity method.

4.7 Ice core measurements of EastGRIP acidity data

Complementing the method optimization and method performance analysis outlined in sections 4.5 and 4.6, the processed acidity data of the EastGRIP core measured during the melting campaign 2019 is showcased in this project. The data processing was performed by the Climate and Environmental Physics group at University of Berne (responsible: Camilla Jensen). Thus the methodological procedure of processing the acidity measurement data, including the calculation of the concentrations based on the established calibration, data correction for contamination or air bubbles, is not covered in this study. Here, extracts of the data set are shown in order to discuss some features of the acidity data that relate to the method performance of the optimized continuous acidity method used during the EastGRIP measurement campaign 2019 (see section 4.2). Further, the sections selected show a broad range of interesting climatic events, such as a relatively big volcanic eruption, several smaller volcanic eruptions close to each other as well as alkaline peaks.

Contrary to the two areas of analysis outlined above (4.5 and 4.6), this part of the study does not base on a strong methodological concept. Rather, the EastGRIP ice core acidity measurements presented serve as an example of the obtained acidity record indicating the volcanic activity at the time. As the acidity record is compared to the meltwater electrolytic conductivity, dust and ammonium CFA data, this provides insight into the state of the climate at that time and thus opens the discussion on areas for further research on the volcanic record.

5. Results

The results are presented as follows: The first two sections present the results of the acidity method optimization. This includes both an assessment of the signal to noise ratio of the optimized Berne setup compared to the Copenhagen setup (5.1), and of the results of the optimization of the dye concentration (5.2). Further, the performance of the optimized acidity method as used during the EastGRIP measurement campaign 2019 is assessed, by investigating the calibration coefficients of the standard data (5.3). Lastly, selected acidity events of the EastGRIP CFA acidity measurement data are showcased as indications for volcanic activity (5.4).

5.1 Restructured acidity setup: method optimization

As part of this study, the optical dye method for acidity developed by Kjær et al. (2016) was optimized. First, the instrument setup was changed as described in section 4.2. A descriptive comparison of two standard runs representing each of the method setups is presented in this section. Second, a dye test was executed with the aim of elevating the instrument's sensitivity by altering the dye concentration. These results are described in section 5.2.

The continuous measurement technique and the difference between the optimized Berne setup and the method developed by Kjær et al. (2016) are described in section 4.2. By means of a descriptive comparison of the two detection instruments, figure 7 shows an exemplary standard run for each of the two systems. For the Berne setup, a standard data file from the first week of measurements of the EastGRIP measurement campaign 2019 (15 Jan 2019) was chosen, whereas the standard data representing the Copenhagen setup stems from the 2018 campaign (17 Mar 2018). It should be noted that the standard sequence do not correspond. Also the detected signal in the Berne setup is given out in voltage, whereas the Copenhagen system reads out the light intensity, thus the strength of the two signals are not directly comparable.

The figure shows the difference in noise produced by the Berne and Copenhagen acidity measurement setups respectively. From the Copenhagen setup in the top part arises a lot more noise compared to the Berne setup. The signal to noise ratio calculated for the HCl 19.4 µM standard amounts to 3.7 for the Copenhagen setup and 141.5 for the Berne setup respectively. The noise is defined as the mean minus and plus two standard

deviations. This difference of a factor of almost 40 is a result of the setup and the respective measurement principles used: The LED with a specific wavelength of 590 nm coupled with an optical band-pass filter in the spectrum of 589 nm enables the detection of acidity at the peak wavelength of 589 nm, leading to low noise levels. Further, the temperature stabilization of the acidity method in the Berne setup controls possible effects of temperature on the measurement principle of the photosensor module. On the other hand, in the Copenhagen setup neither of these elements are implemented. Therefore, the spectrometer used is influenced by temperature fluctuations leading to more noise in the detected acidity signal.

As outlined in section 4.4, the signal to noise ratio of a detection system is of high importance when assessing a method or instrument (Bigler 2000). Maximizing the signal to noise ratio by either reducing the noise or elevating the signal, the quality measures of the acidity method can be improved. On the basis of a strictly descriptive assessment, thus, the Berne setup outperforms the Copenhagen setup by means of lower noise production.
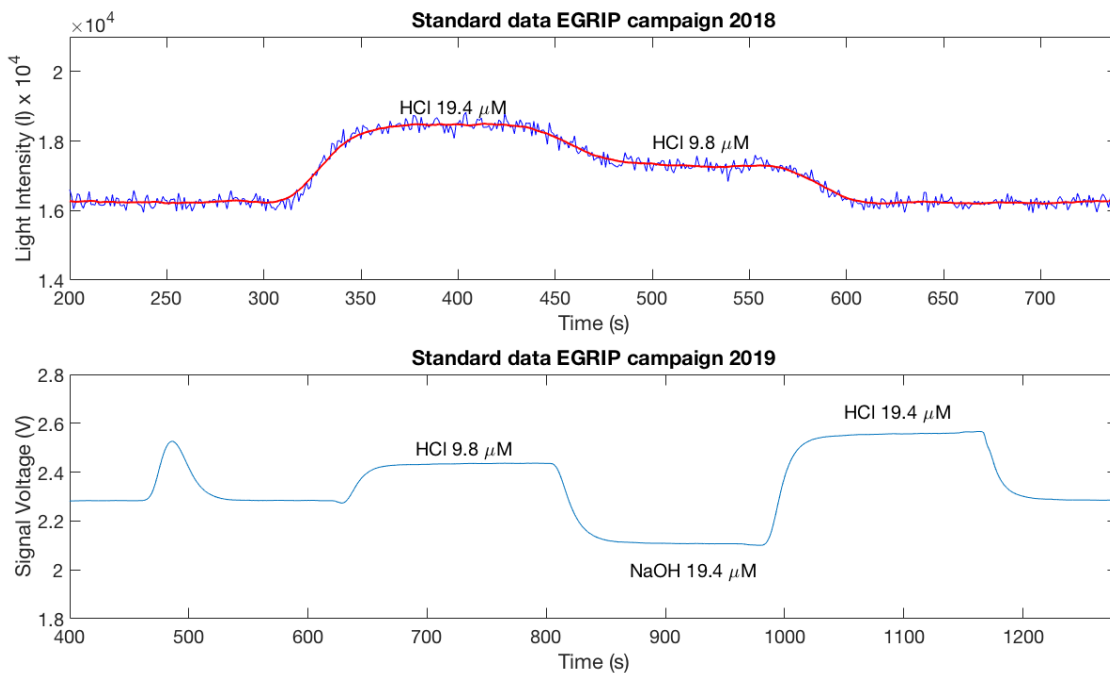
Figure 7: Descriptive comparison of the signal to noise ratio of two standard runs. The top figure shows an example of a standard run from the EastGRIP campaign 2018 with the Copenhagen instrument setup as described by Kjær et al. (2016). The data is from 17 March 2018. The blue line shows the detected light intensity (I) at 586 nm with the red line representing the smoothed signal. The bottom figure shows an example of a standard run in the EastGRIP campaign 2019 with the optimized setup, here called Berne setup. The standard data is from the 15 January 2019 in the first week of measurements.

5.2 Dye test: method optimization

The dye test conducted is aimed at investigating and optimizing the dye concentration of the reagent used for the acidity method that was employed during the EastGRIP measurement campaign 2019. While Kjær et al. (2016) already tested different dye concentrations, the test included changing both the dye concentration and the ratio of the two indicator dyes at the same time. To complement their obtained results, the dye test in this study specifically investigated the impact of the dye reagent concentration on the method performance alone.
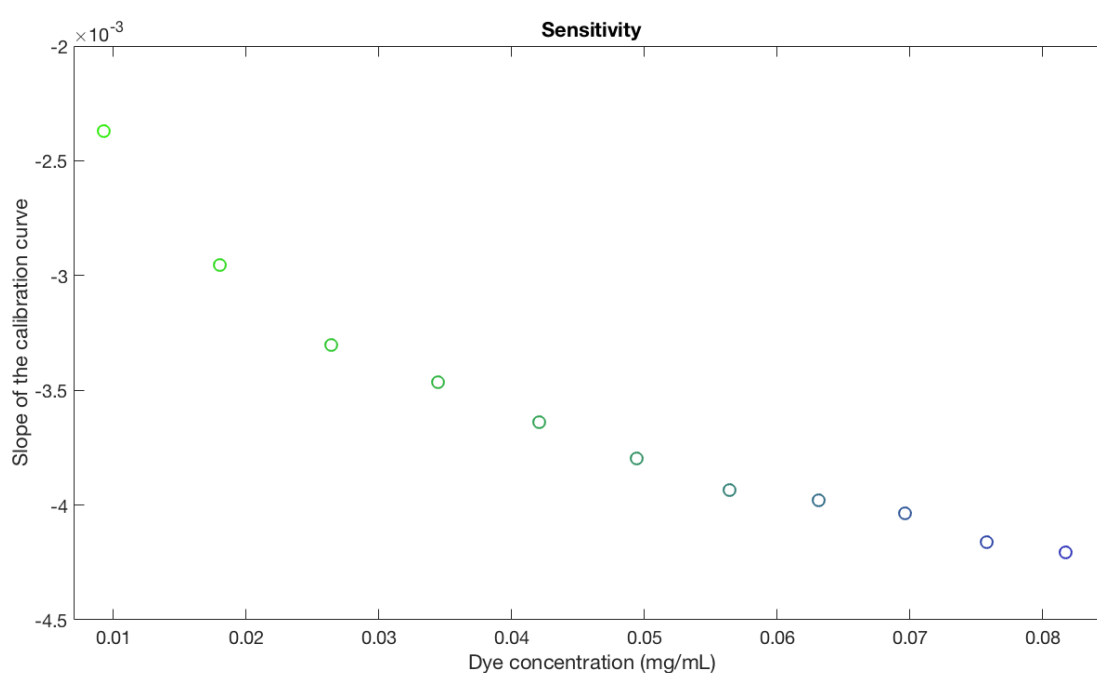

Figure 8: The slope of the calibration curve of the different dye concentrations, as a measure of their respective sensitivity. The steeper the slope of the calibration curve, the higher the sensitivity of the method. The colors of the markers indicate the dye concentration.

The effect of the different dye concentrations on the sensitivity of the instrument was investigated by assessing the respective slopes of the calibration curves (figure 8). As seen in figure 9, the relationship between the slope of the calibration curve and the dye concentration follows an exponential curve with two bases and two times the dye concentration in the exponent. It can be hypothesized that this form of the fitted curve could be a result of the two indicator dyes being used for the detection of acidity. This negative exponential relationship means that the change in the slope of the calibration curve for incremental changes in the dye concentrations is high for low dye concentrations and low for high dye concentrations. Thus, higher concentrations

correspond with a steeper slope of the calibration curve, in turn corresponding with a better response of the instrument. However, there is a decreasing gain in the method's sensitivity with increasing dye concentrations. This can be assumed to be a saturation effect. With increasing dye in the reagent, the sample gets darker up to a point where additional dye does not further improve the acidity detection. This hypothesis is supported by the fact that when plotting the dye concentration on a logarithmic scale, the relationship between the concentration and the slope of the calibration curve becomes more linear, as seen in the bottom panel in figure 9. However, the figure shows that the two lowest dye concentrations deviate from the linear relationship between the log of the slope of the calibration curve and the dye concentration.
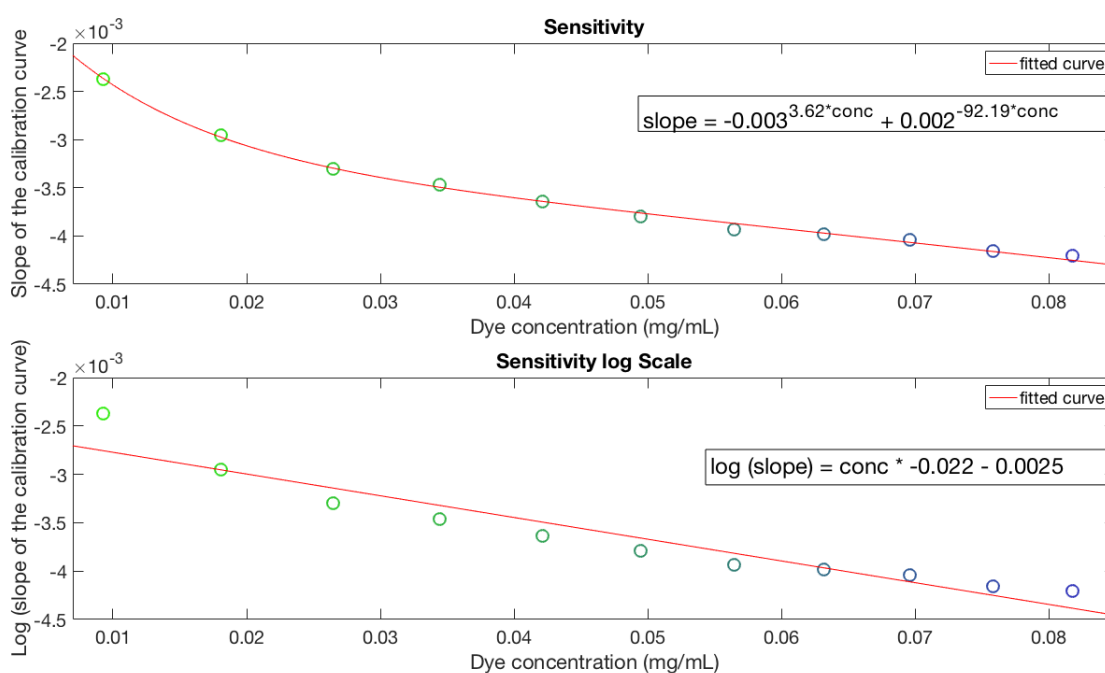
Figure 9: Sensitivity of the different dye concentrations on a linear scale (top) and on a log scale (bottom). The fitted curve in the top is of a negative exponential form, while in the bottom panel it is a linear polynomial curve. The dye concentration in the shown form of the fitted curve is abbreviated with "conc".

In addition to the sensitivity offered by the respective dye concentration, the level of the baseline is a second factor determining the optimal dye concentration for the continuous detection of acidity. Figure 10 shows the voltage signal for the two baselines, baseline 1 before, and baseline 2 after the standard run, for the different dye concentrations. The baseline signal is important as it determines the area of the method's sensitivity. If the baseline is chosen too low, the risk arises of not measuring the alkaline signal, with the sample being too dark for the detection of acidity. The Berne setup includes a photomultiplier that offers some room for adjustments of the baseline. However, it is

reasonable to assume that both the LED and the photomultiplier used in the acidity method setup wear out over time, leading to lower acidity signals being detected. Hence, it is assumed that a decrease in the emitted light intensity of the LED and a decrease in the detection of the photosensor induce a small linear downward drift of the baseline over time. This thus strengthens the argument to select a dye concentration from the middle range tested in the underlying dye test.

Lastly it has to be noted that the two parameters investigated, the slope of the calibration curve and the baseline, are not independent. As the absorption calculation used for producing the calibration curve is a relative measure of the baseline plus the response of the standard solution divided by the baseline. This results in steeper slopes for lower baselines.
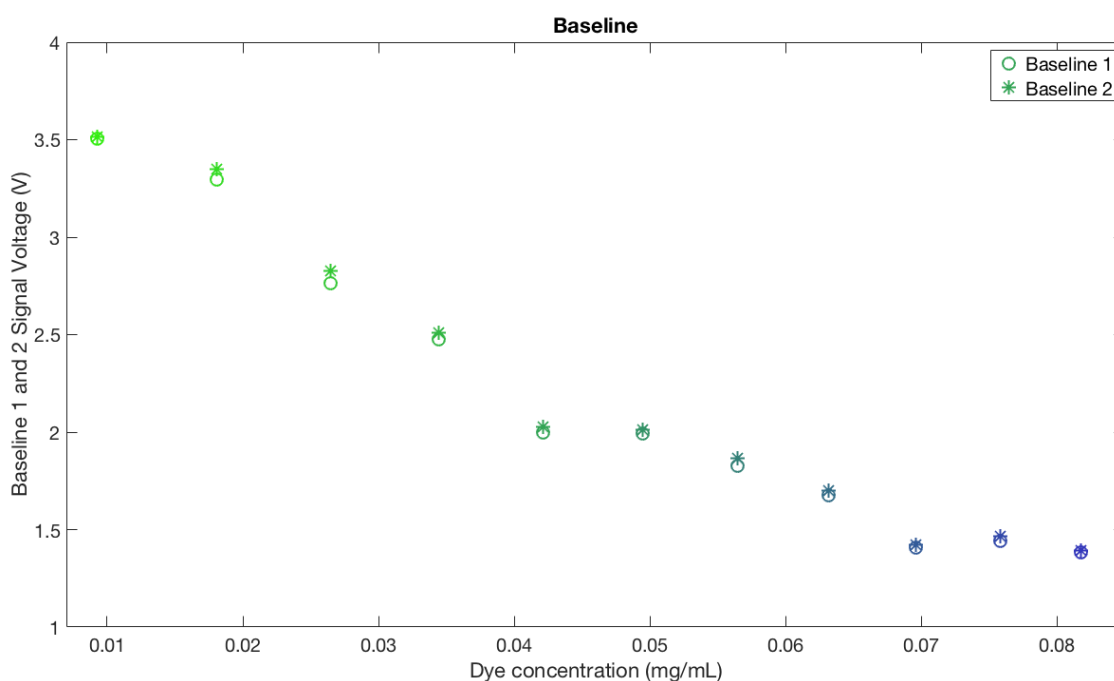
Figure 10: Baseline in signal voltage (V) for the different dye reagent concentrations. Baseline 1 represents the MilliQ signal before the start of the standard series, while Baseline 2 refers to the MilliQ signal after the end of the standard series.

It can be concluded that first, the optimal dye concentration should lie in an area of high sensitivity. Thereby, the dye concentration should be chosen in an area where incremental changes in the concentrations do not lead to big changes in the response of the method. This is true for stronger dye concentrations. However, it is equally important that a dye concentration is opted for that offers a baseline that is not too low.

In addition, the response time of the different dye concentrations as a measure for the temporal resolution of the method is shown in figure 11. The response time, in this study, is defined as the time (s) required for the signal to go from 10 % to 90 % of the peak response between the MilliQ baseline and the standard solution as well as between the three standard solutions. A 10 % to 90 % response time was used, instead of a 5 % to 95 % response time, in order to decrease uncertainties induced by air bubbles seen in the data. It can be assumed that the four different response times vary systematically in line with the different responses between the standard concentrations and the MilliQ baselines. This is represented by the spread between the different response times for the different dye concentrations.
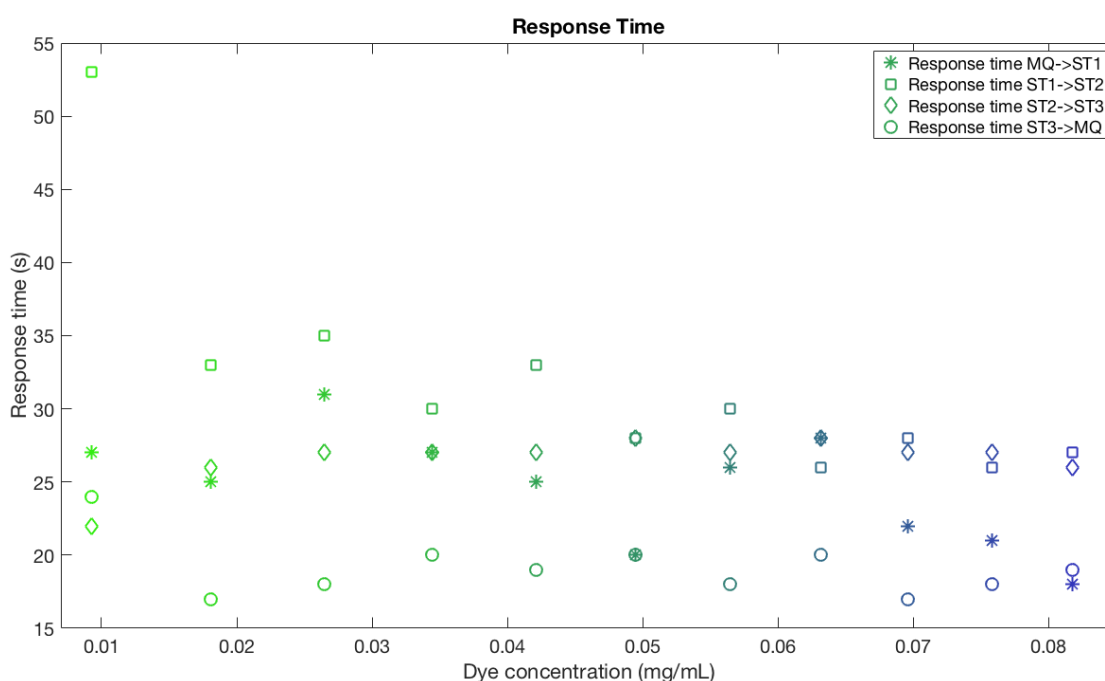
Figure 11: Response time of the different dye concentrations, measured as the time (s) it takes the signal to go from 10 % to 90 % of the peak response between baseline and the standard solution as well as between the different standard solutions. Thereby, the response time MQ->ST1 refers to the change from the MilliQ baseline to the first standard (NaOH 9.8 µM), response times ST1->ST2 and ST2->ST3 refer to the changes from standard 1 to standard 2 (HCl 19.5 µM) and from standard 2 to standard 3 (NaOH 19.4 µM) respectively. Response time ST3->MQ means the change from standard 3 again to the MilliQ baseline.

Generally, figure 11 shows that the temporal resolution is better with stronger reagents, as the spread between the different response times decreases for stronger dye reagents. Especially the response times MQ->ST1 and ST1->ST2 decrease for higher dye concentrations, while the response times ST2->ST3 and ST3->MQ are on a similar level for the different dye concentrations. This is highlighted by the variability of the four response times in table 7, showing that the standard deviations of the response

times MQ->ST1 and ST1->ST2 are bigger than for ST2->ST3 and ST3->MQ. The higher standard deviation of response time ST1->ST2 can thereby be ascribed to the outlier in the weakest dye concentration. Except for three instances, the response time ST3->MQ shows the fastest response. In line with this and its low variability it has the lowest mean response time of 19.09 s.

Table 7: Variability of the four response times dependent on the different dye concentrations: mean response time (s) and standard deviation (s) for the four different types of respond times.

	Mean response time (s)	Standard deviation (s)
Response time MQ–>ST1	24.55	3.88
Response time ST1–>ST2	31.72	7.66
Response time ST2–>ST3	26.55	1.63
Response time ST3–>MQ	19.09	1.97

Both quality criteria assessed by means of optimizing the dye reagent concentration for the new acidity method setup used in the EastGRIP measurement campaign 2019 show better results for stronger concentrations. First, stronger dye concentrations give a better response measured by the slope of the calibration curve. And second, the response time is shorter for stronger dye concentrations; this holds true for the response times MQ->ST1 and ST1->ST2. Thus, based on the response time only, the optimized setup of the optical dye method for acidity should in opt for strong reagents. Taking into considerations the results on the sensitivity and the baseline, figures 9 and 10, the optimal dye concentration should be chosen around a concentration of 0.04 mg/mL to 0.06 mg/mL.

Two limitations are discussed with regards to the analysis of the dye test. First, as outlined in section 4.5, the different reagents were run only once due to time restrictions. Therefore the results must be interpreted with caution; a bigger data set would have strengthened the reliability of the results. Second, an effect of the order the different reagents were run in cannot be ruled out: A strong reagent run before a weaker one might slightly increase the dye concentration of the latter. In between the different reagents MilliQ water was run through the system, though, the system was not extensively cleaned out in between the different runs. However, with a random order of the different concentrations, this effect was randomized.

After this first part assessing the leeway for a further optimization of the dye reagent concentrations, the investigation follows of how the optimized acidity method setup performed during the EastGRIP measurement campaign 2019.

5.3 EastGRIP campaign: method performance

The EastGRIP measurement campaign 2019 standard run data is evaluated, in order to investigate the performance of the optimized continuous acidity method over the whole duration of the campaign. Thereby, all standard data was discarded where the variables of interest, such as the slope or the intercept of the calibration curve or the calculated absorption values, exceeded two standard deviations. For outliers of this scale it can be assumed that the standard concentrations were off due to poor preparation. A resulting data set of 211 standard data files is used for the subsequent method performance analysis.

As a basis for the following assessment of the method performance by means of different quality criteria, first of all this study looks into the variability of the calculated absorption of the three standard solutions over the course of the EastGRIP measurement campaign 2019 (figure 12). The distribution of the absorption thereby gives an indication of how well the standard solutions were prepared, as ideally their concentration and thus absorption is constant over time. In section 4.3 a theoretical uncertainty range for the standard solutions was calculated resulting to 4.93±0.13 μM and 9.80±0.25 μM for the low and high standards respectively. This uncertainty range does not include systematic errors induced by the person preparing the standard solutions. It only includes the variability of the volume for both the MilliQ water and the chemistry induced by inaccuracies of the pipetting and the MilliQ water measuring system.

Figure 12 shows three histograms of the distribution of the calculated absorption for the HCl 4.93 μM, NaOH 9.80 μM and HCl 9.80 μM standards, with the mean and the standard deviation for the fitted normal distribution shown in the respective boxes. The figure shows only the standard runs after the standard concentrations were changed (see section 4.3), as the section before changing the concentrations only counts around 30 data files. The figure shows that the variability of the calculated absorption is higher for the high standards – both HCl and NaOH – compared to the low HCl standard. The variance (σ^2) of the three absorption distributions, as a measure for the spread of the

probability density around its center, is approximately twice as big for the high NaOH 9.80 μM and three times bigger for the high HCl 9.80 μM standard than the low HCl 4.93 μM standard.

The result of a higher variability for the high standard concentrations is in line with the higher calculated theoretical uncertainty range for the high standards, resulting from a higher random variability in the pipetted volume of the chemistry. On the basis of this descriptive result, it can thus be argued that the variability of the standards is reasonable, arguing for a consistent preparation of the standard solutions over the course of the EastGRIP measurement campaign 2019.
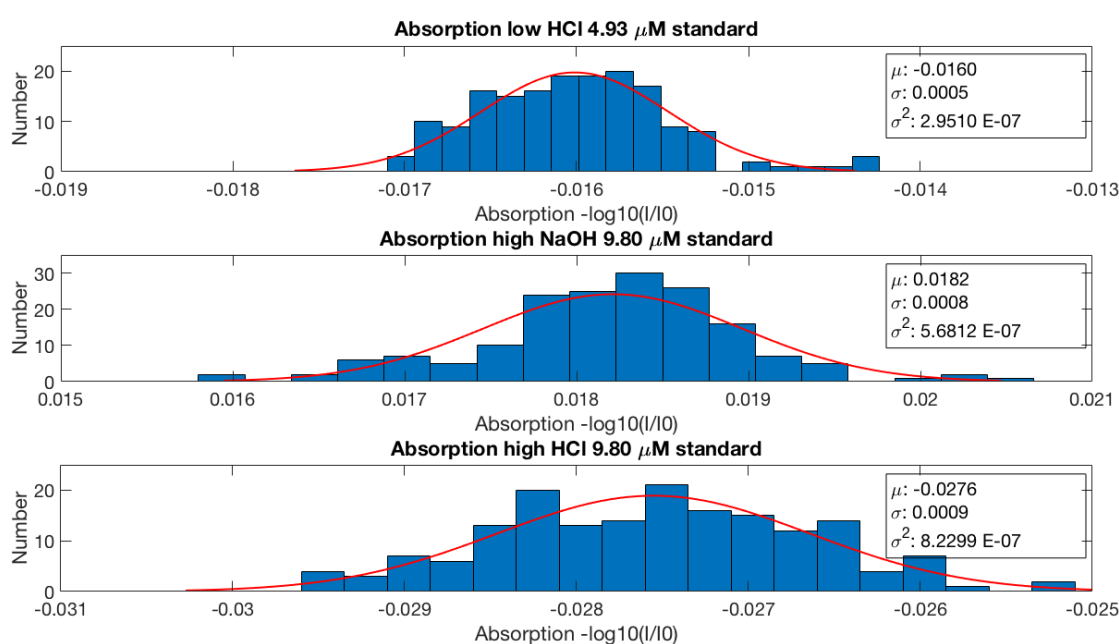
Figure 12: Histograms of the distribution of the calculated absorption for the HCl 4.93 μM, NaOH 9.80 μM and HCl 9.80 μM standard solutions. Only standard runs from after the standard concentrations were changed are shown. The red line shows the Gaussian fit for the respective distribution, with the mean (μ), the standard deviation (σ) and variance (σ^2) for the respective normal fit shown in the added box.

Further, different calibration options were assessed and compared. Figure 13 compares the slope of the calibration curve of different scenarios: including both NaOH and HCl standards compared to including only NaOH in producing the calibration curve with and without forcing the calibration curve through zero. As the slope of the calibration curve together with the precision controls the sensitivity of a detection method, a steep slope refers to a high sensitivity (Bigler 2000).
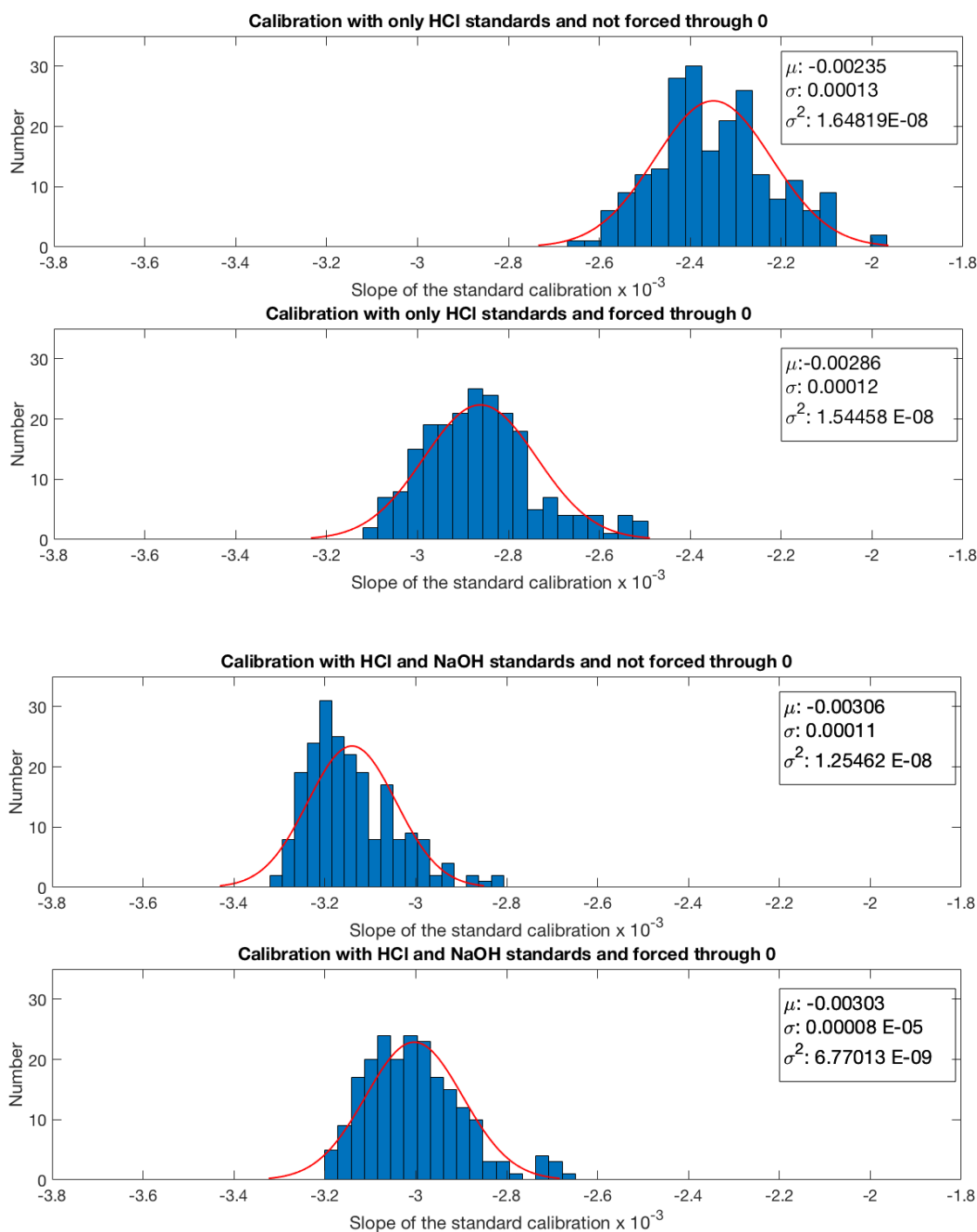
Figure 13: Distribution of standard calibration slopes for different calibration scenarios. The first row shows the distribution of the slopes for a calibration with the acid standards only and without forcing the calibration curve through zero. The second row shows the distribution of the slopes also for a calibration with the acid standards only but while forcing the calibration curve through zero. Rows three and four show the distribution of the slopes when including both the acid and alkaline standards with the curve not forced through zero (3) and forced through zero (4) respectively. The red line represents the normal fit for the respective distribution.

From the descriptive comparison in figure 13 it can be seen that the calibration done with both the HCl and NaOH standards result in steeper slopes of the calibration curve. The steepest slopes thereby result from not forcing the calibration curve through zero.

45

The two calibration methods with only the HCl standards both show less steep slopes of the calibration curves, with the situation of the curve not being forced through zero giving the least steep slopes. This shift in the slope of the calibration curve between not forcing and forcing it through zero as well as between including only HCl standards and including both HCl and NaOH standards will be discussed in more detail further below.

Onward, the assessment of the method performance focuses on the calibration coefficients over time, specifically on the slope of the calibration curve as a measure for the sensitivity of the acidity method as well as the intercept. Figure 14 presents an example of three calibration curves for data from the EastGRIP measurement campaign 2019: one example each from the beginning, the middle and the end of the campaign. This selection covers both a standard run with the original standard solution concentration, in magenta, and two runs after the concentrations were halved, in black. The uncertainty ranges for the standard concentration and the calculated absorption are given in horizontal and vertical error bars respectively, however, they are mostly within the range of the marker size used in this plot. The uncertainty ranges for the concentration of the standard solution results from the variability in the volume of the pipetted solutions as well as the MilliQ water used to prepare the standard solutions (see table 4 in section 4.3). The uncertainty in the calculated absorption, on the other hand, results from the noise in the acidity signal. Thus, this uncertainty can vary from run to run.

Further, figure 14 shows both the calibration curves including only the HCl standards (blue solid line) as well as the calibration curves including both HCl and NaOH standards (red dashed line). This illustrates the difference in the steepness of the slope between these two calibration methods also seen in figure 13 above. As also seen in figure 6, section 4.2, there is a non-linear relationship between the $-\log10(I/I_0)$ of the HCl and NaOH standard concentration, resulting in different calibration curve slopes when fitting the linear calibration curve only to the HCl standard absorption values compared to both the HCl and NaOH values (seen in figure 13 and 14). Also, when the calibration curve is not forced through zero, this results in a shift in the intercept when changing the standard concentrations, as also discussed further below. To this end, Kjær et al. (2016) produced separate linear regressions for the HCl and NaOH standards. This study, however, used a linear gradient including both the NaOH and the HCl standards, introducing a higher uncertainty for the subsequent calculation of the sample

concentrations. However, most of the sample concentration is assumed to be in the acid range and the linear fit is better for the HCl standards as there are more standard data points available. Thus, for the acid range represented by the HCl standard concentrations, the calculation of the sample concentration is assumed to still be adequate. More generally, however, the selection of three standard calibrations from the beginning, middle and end of the campaign opens up for the comparison of the calibration over time.
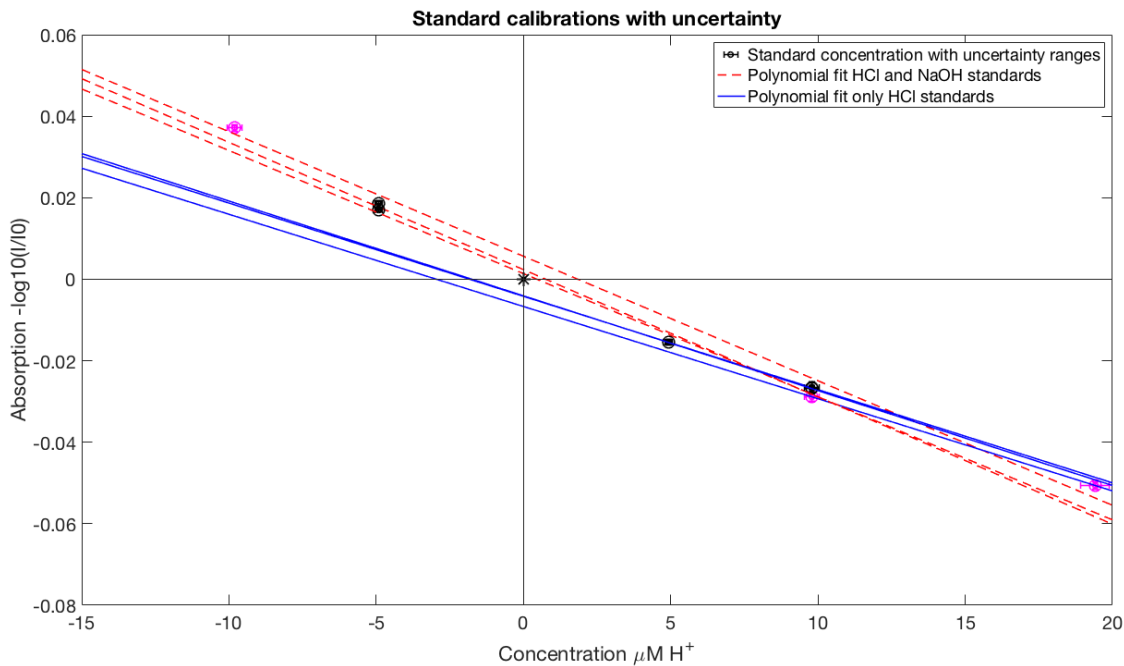

Figure 14: Three examples of the standard calibrations and the resulting standard calibration curves, representing each a run from the beginning, the middle and the end part of the EastGRIP measurement campaign 2019. The dots mark the concentration vs. the calculated absorption used to produce the calibration curve before (magenta) and after (black) the standard concentrations were halved. In the same color, uncertainty ranges for the standard concentration and the calculated absorption are given in horizontal and vertical error bars respectively. The blue solid line shows the calibration curve only including the HCl standards, whereas the red dashed lines include both the HCl and NaOH standards. All calibration curves are not forced through zero. The NaOH concentrations on the x-axis are referred to as a negative H^+ concentration.

To this end, figure 15 shows the all calibration curves over the whole EastGRIP measurement campaign 2019. This allows for a comparison of the slopes of the calibration curves over the whole campaign. As the individual curves are plotted transparently, the darker the area the more calibration curves lie in this area. Again, the standard data before (red) and after (blue) the standard concentrations were halved can be distinguished. It seems that the change of the concentrations results in a subsequent slight shift towards steeper slopes of the calibration curves. This is true for the case of the calibration curve being forced through zero. In the other case, with the calibration

curve not being forced through zero, it can be seen that after halving the standard concentrations, the intercept shifts towards zero. These changes in both the slope and the intercept over time will be discussed in more detail further below.
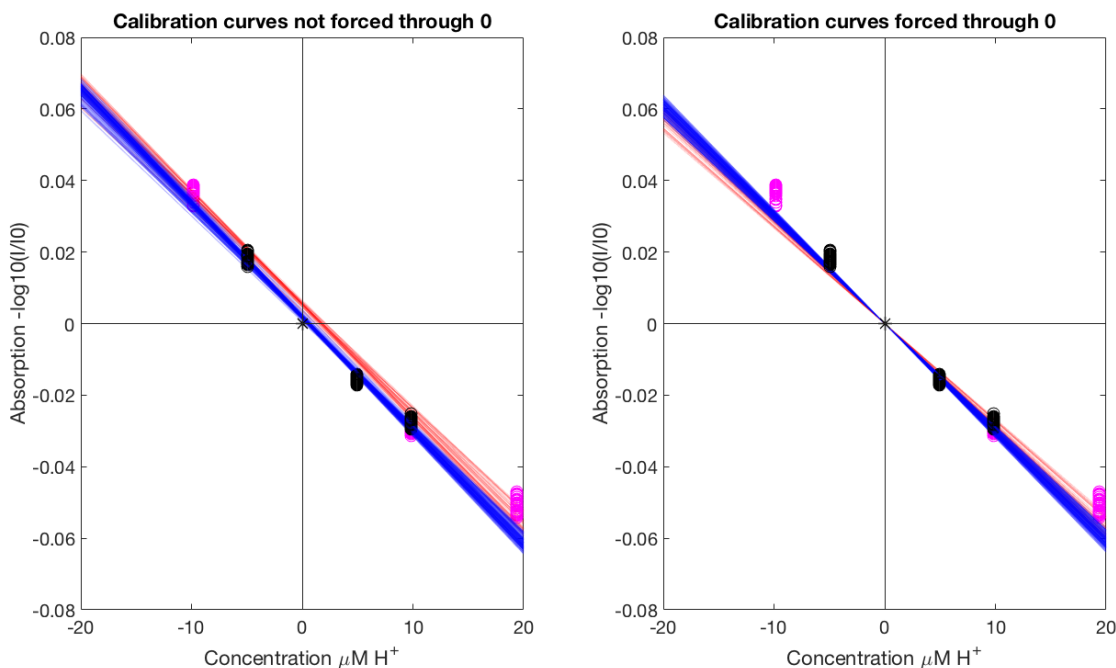

Figure 15: Linear calibration curves of all standard data over the course of the EastGRIP measurement campaign 2019. The left panel shows the calibration curves not forced through zero with a subsequent intercept on the y-axis. The right panel shows the calibration curves forced through zero. Both calibration methods include both the HCl and NaOH standards. In red are the calibration curves from the standard data before and in blue after the standard concentration were halved. The calibration curves are made transparent in order to allow the visualization of the distribution of the curves to a certain degree. The magenta and black dots mark the concentration vs. the calculated absorption used to produce the calibration curve before and after the standard concentrations were halved respectively.

Overall, the figure shows that the slopes of the calibration curves are relatively constant over the course of the EastGRIP measurement campaign 2019, suggesting a good performance of the method. In the following figures, the performance of the method over time will be investigated in more detail.

Figure 16 shows the slope of the calibration curves over the time period of the EastGRIP measurement campaign for both methods with (top panel) and without (bottom panel) forcing the calibration curve through zero. Thereby, the form of the scatter of the calibration slopes looks similar for both versions, with and without forcing the calibration curve through zero. Again, as already seen in figure 13, the calibration curves not being forced through zero yield slightly steeper slopes, as can be seen on the dashed lines indicating two standard deviations below and above the mean over all calibration slopes. Further, this descriptive analysis does not show systematic

differences in the slope of the data points where the calibration was produced manually with exceptions in the automated matlab script. Thus it can be assumed that the manual calculations perfomed well and in consistence with the automated script.
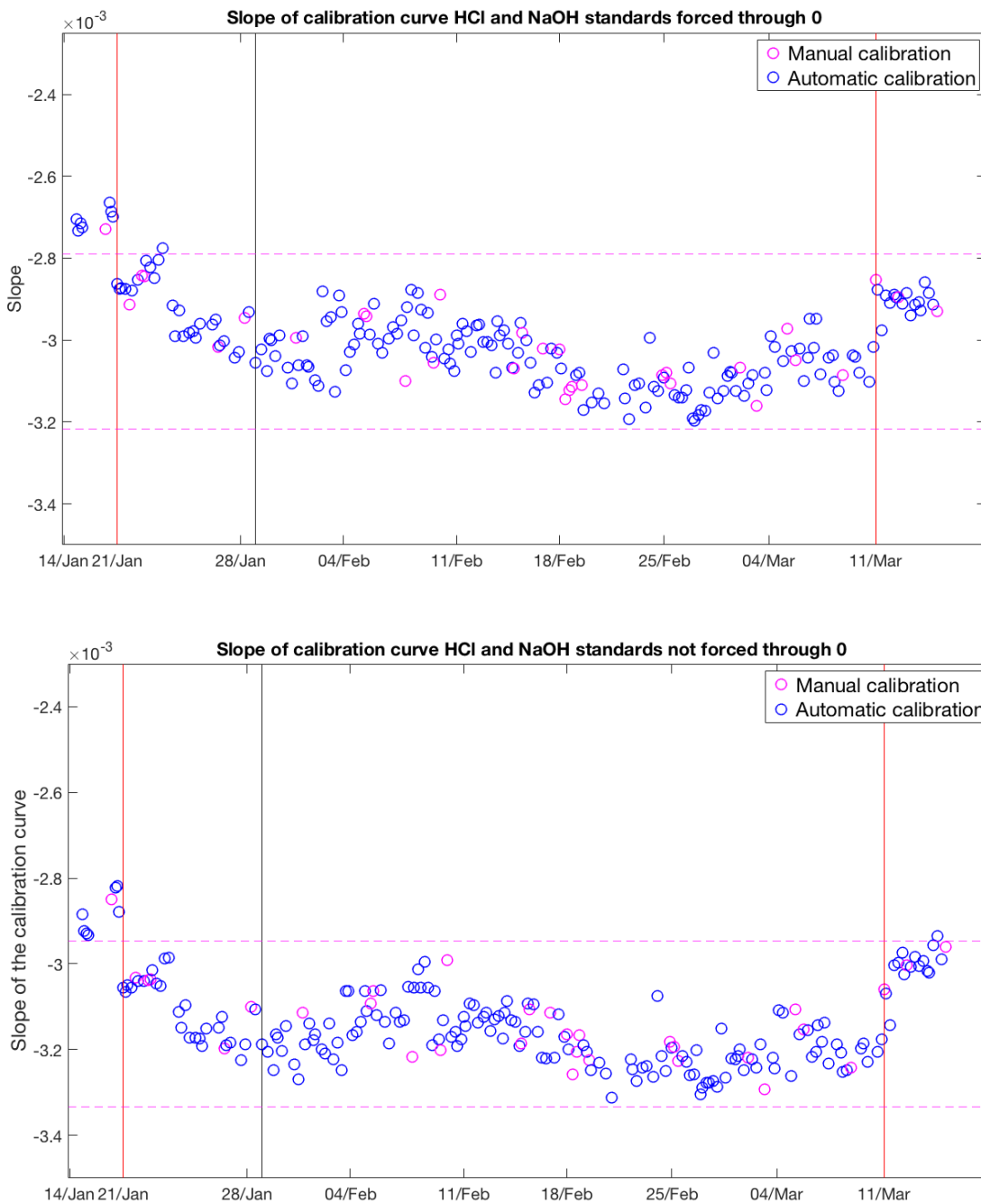
Figure 16: Standard calibration slopes including both HCl and NaOH standards over time, with the magenta dashed lines marking the range of two standard deviations below and above the mean over all calibration slopes. The top panel shows the calibration slopes when forcing the calibration curve through zero, while the bottom panel shows the calibration curves when not forcing the calibration curve through zero. The pink markers represent data calibrations where the baselines and/or the standard values were defined manually. The dates on the x-axis mark all the Mondays during the EastGRIP measurement campaign 2019. The black vertical line marks the date when the standard calibration concentrations were halved (28 Jan 2019) and the red lines mark the dates when a new stock reagent was used.

Two main things can be taken from figure 16. First, it can be seen that except for the first and last few days, the slopes of the calibration curves are more or less constant over time. However, a fluctuation between steeper and less steep slopes of the calibration curves can be observed. This cannot be the result of the temperature as the acidity system is held at a constant temperature. Neither can it be induced by the LED or the photosensor module wearing out over time, as it can be assumed that these components of the system setup would induce a linear effect on the sensitivity. Similarly, if the observed fluctuations were induced by the stock reagent wearing off, a change towards less steep slopes of the calibration curves over time would be expected. On the basis of this descriptive analysis, this study thus argues that these fluctuations could result from a combination of the variability in the standard preparation and the tubing of the acidity system. The latter might have induced small changes in the flow of the sample and dye reagent leading to changes in the mixing ratio of the sample and dye reagent.

Second, two clusters at the beginning and end of the campaign exhibit less steep calibration slopes that are close to or even exceed two standard deviations above the mean over all calibration slopes. With the melting campaign starting on 21 Jan 2019, the first few datasets represent standard runs from the setup of the CFA and acidity system. For these first standard runs, an old stock reagent from Dec 2018 was used. On 17 Jan 2019 a new stock reagent was prepared and first used in the acidity system on 21 Jan 2019 as indicated by a vertical line in figure 16. Another new stock reagent was used for the last week of the melting campaign starting on 11 Mar 2019, again indicated by a vertical line. On the basis of figure 16 it can be argued that the two step changes in the calibration slopes are in line with a new stock reagent being used both at the beginning and end of the campaign. As no other changes occurred at these two times – based on the information available – this study postulates that the less steep calibration slopes might have been induced by the reagent. However, it is unclear why the new stock reagent results in less steep calibration slopes, as one would assume that a new reagent initially leads to a stronger response of the acidity system and then wears off over time.

Further, it can be assumed that the deviant calibration coefficients from before the start of the measurement campaign (before 21 Jan 2019) are a result of an old stock reagent used as well as different factors of the CFA being changed during the setup week. It is

thus reasonable to assume that the standard calibration data obtained during the campaign setup (before 21 Jan 2019) is not representative.

As outlined in section 4.6, towards the end of the campaign (04 Mar 2019) the reagent used was prepared with a little less stock solution, lowering the concentration compared to the other weeks. On the basis of these results, however, the slightly lower concentration did not result in a lower slope of the calibration curves. This strengthens the conclusion of the dye optimization analysis (section 5.2) that a dye concentration should be chosen so that incremental changes in the concentration should not lead to big changes in the slope of the calibration curve. This is thus the case for the optimized dye reagent concentration used during the EastGRIP measurement campaign 2019 of 0.05 mg/mL.
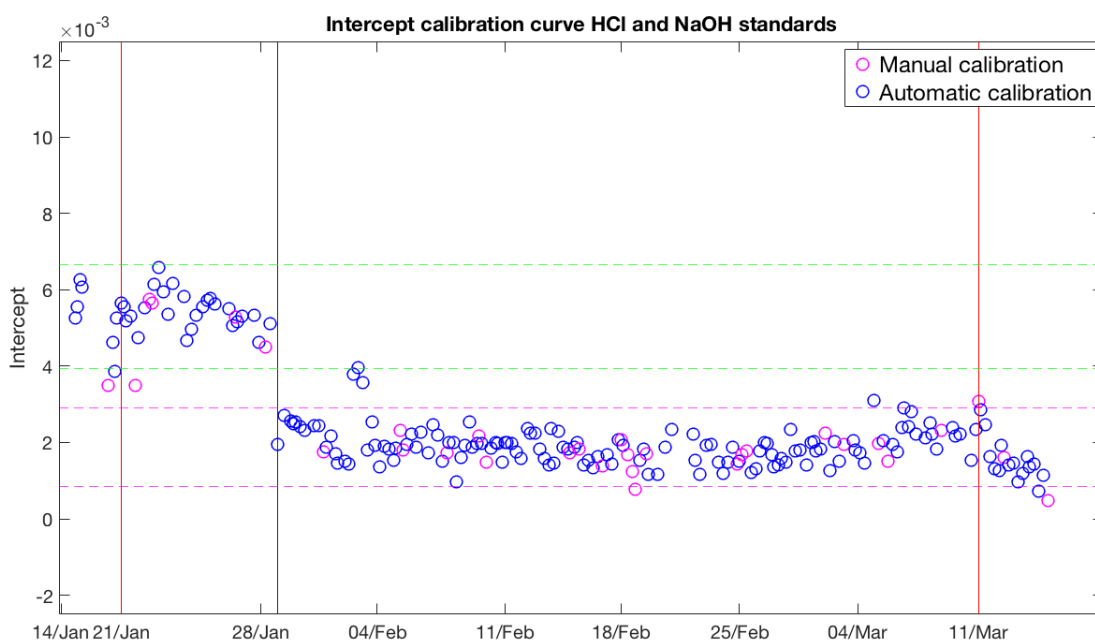

Figure 17: Intercepts resulting from the calibration of both HCl and NaOH standards when not forcing the calibration curve through zero. The pink markers represent data calibrations where the baselines and/or the standard values were defined manually. The green dashed line indicates two standard deviations above the mean of all intercepts before the standard concentrations were halved, while the magenta dashed lines indicate the corresponding range after the standard concentrations were halved. The dates on the x-axis mark all the Mondays during the EastGRIP measurement campaign 2019. The black vertical line marks the date when the standard calibration concentrations were halved (28 Jan 2019) and the red lines mark the dates when a new stock reagent was used.

Lastly, the intercepts of the calibration curves when not being forced through zero are shown in figure 17 over the time of the EastGRIP measurement campaign. The intercept is shown for the calibration including both HCl and NaOH standards. Similar to the analysis of the slope over time shown above in figure 16, no systematic deviation of the

51

data points where the calibration was produced manually from the automated calculations of the intercept can be observed here. This strengthens the postulation made above that the manual calculations were performed in consistence with the automated script.

Two main observations of figure 17 are discussed here: First, the variability of the intercepts before the standard concentrations were halved is higher compared to after. The change of the standard concentrations is indicated by the vertical black line. Except for a few outliers in the beginning and a downward trend in the end, the intercepts after the concentrations were changed, are quite constant over time. The reason for the higher variability before the standards were halved cannot be inferred from this analysis. As seen above, also the slopes of the calibration curves show up as deviant in this descriptive analysis during this time in the measurement campaign. Similarly as argued above, it is reasonable to assume that this again might be induced by the dye reagent.

Second, the change of the standard concentrations marks a shift in the intercept towards zero. This was already discussed with reference to figure 15. Not shown here, this is also true when only the HCl standards are included to produce the calibration curve. The reason for this intercept shift towards zero is again the non-linear relationship between the $-\log 10(I/I_0)$ of the HCl and NaOH standard concentrations. This results in different calibration curve slopes when fitting the linear calibration curve only to the HCl standard absorption values compared to both the HCl and NaOH values.

This concludes the results of the method performance during the EastGRIP measurement campaign 2019. Next, moving on from the calibration data, indications of volcanic activity in the EastGRIP measurements are presented and discussed.

5.4 EastGRIP campaign: ice core acidity measurements

The processing of the EastGRIP data from the measurement campaign 2019 was performed by the Climate and Environmental Physics group at University of Berne. The analysis of the method performance of the acidity method used during the EastGRIP measurement campaign 2019 is thus constrained to the standard data analysis presented in the previous section. However, the main method performance issues as observed during the data processing are discussed here. As these observations on the acidity method performance were only personally communicated and discussed with the

Climate and Environmental Physics group at University of Berne, no documentation of any kind can be shown here.

Overall, the acidity baseline has shown to be rather unstable: In some of the measurement data runs a downward drift was observed, with the extent of the drift varying from run to run. The drift can be determined as the difference between the baseline before and after the measurement run and was thus corrected for by linear interpolation of the signal. Ideally, the baseline of a detection technique is stable throughout up to several meters of the ice core measured. However, the acidity method is highly sensitive to the mixing ratio of the sample and the dye reagent. Therefore, a drift can be expected as a result of unequal wear-out of the tubing. As a reference point, a conservative assessment of the uncertainty induced by drift during ice measurement runs put forward by Kjær et al. (2016) is approximately 0.20 ± 0.25 µM H^+ (6.5 %). However, this estimate is setup-specific and the uncertainty inferred by drift in the Berne setup as used during the EastGRIP measurement campaign 2019 would need to be calculated. Also, as discussed in section 5.3, the ageing of the reagent might induce drift (Kjær et al. 2016). Further, after each run a shift in the acidity baseline can be observed. The actual reason for this baseline shift is unknown. However, it can be argued that it might be in response to a change in one of the other systems that were on the same manifold as the acidity instrument. For the processing of the measurement data this means that the baseline before the shift can be assumed to be more representative (personal communication, Camilla Jensen and Tobias Erhardt, 2 May 2019).

The data presented in this section ranges from 544.50 m to 548 m depth (figure 18) and 580.5 m to 587.5 m depth (figures 19 and 20). This section showcases a selection of the EastGRIP acidity data on a depth scale, covering a range of different interesting acidity events. In figures 18, 19 and 20, the acidity record is shown in comparison to the meltwater electrolytic conductivity, dust, calcium and ammonium CFA data, providing insight into the state of the climate at that time and pointing towards interesting areas of future research with this data set. Note that the y-axis values differ for the three figures. The presented results of the acidity measurements are thereby only for illustration purposes, no further analysis was performed with the data.

The meltwater electrolytic conductivity, as well as the electrical conductivity and dielectric profiling (see section 3.3) are all related to the H^+ concentration of the sample in some way. Thus in a lot of cases, significant positive correlation coefficients are

found for the H^{+} concentration and EMWC, EMC or DEP (Kjær et al. 2016). The EastGRIP ice core acidity data presented here also accords well with the EMWC signal. This is true for the acid spectrum, with all acid events indicating volcanic activity showing up in both proxies. In these instances, the EMWC signal is mainly determined by the high H^{+} concentration, with other ions in the sample being insignificant.

The acidity data presented further shows a good correspondence with ammonium (NH_4^+). In Greenland ice cores, large peaks in ammonium indicate boreal forest fire events (Legrand and Mayewski 1997, Kreutz and Koffman 2013). The acidity signal, in turn, shows alkaline dips in line with the ammonium peaks. For example, in figure 18 three distinct ammonium peaks are well aligned with three dips in the acidity record.
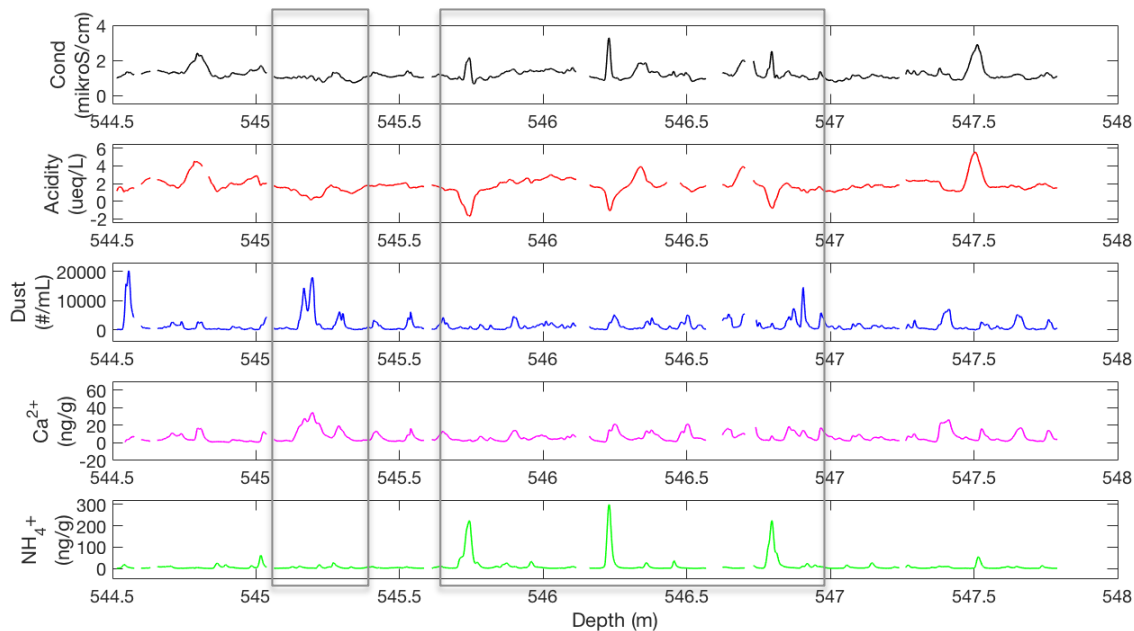

Figure 18: EastGRIP CFA data ranging from 554.5 m to 548 m depth, showcasing a high dust peak coinciding with an acidity dip as well as the correspondence of three ammonium peaks and acidity dips. Electrolytic meltwater conductivity (black), acidity (red), dust (blue), calcium (purple) and ammonium (green) are shown from the top to the bottom panel. Events of interest are highlighted with grey rectangles.

As insoluble dust particles are assumed to interfere with the light intensity measurement of the acidity detection system and to indicate possible contaminations from drill liquid, dust is also shown in the figures 18 to 20. Theoretically, dust particles are to reduce the light intensity detected in the absorption cell, lowering the acidity signal. This matrix effect has not been tested in this study and the data presented in the figures below do not show a systematic pattern between the dust and acidity signals as determined descriptively. However, around approximately 545.25 m depth in figure 18, a high dust

peak coincides with a low acidity signal, in line with the expected influence of dust on the acidity signal. Further analysis and quantification of this matrix effect would need to be conducted. As dust records show dramatically higher concentrations of a factor of 20 and 10 in central Antarctica and Greenland respectively in glacial climates compared to interglacials, dust might constrain the usability of the optical acidity method.

Volcanic eruptions show up in the acidity record as signal peaks. When comparing the different volcanic eruptions shown in the figures below, it has to be noted that the y-axis ranges differ. On a strictly descriptive evaluation, in figure 18 four volcanic eruptions and in figure 19 one big eruption and possibly three to four small volcanic eruptions can be detected. The interpretation of the acidity signal in figure 20 is a bit less straightforward. Thereby, the acidity peak cut off at the end might represent the beginning of a volcanic signal – and so might also the sharp acidity peak at approximately 585 m depth. The acidity signal at 585 m depth is of particular interest as it coincides with peaks in all of the other signals shown: MWEC, dust, calcium and ammonium. A similar pattern of peaks in all of the measured impurities was observed by Bonne et al. (2015) for the melt layer – determined by visual stratigraphy– of the 2012 Greenland summer heat wave. On the basis of this it can be argued that the pattern seen at 585 m depth might indicate a melt layer in the ice, leading to the accumulation of the different impurities at this depth.

The big volcanic eruption shown in figure 19 at approximately 583.3 m depth is in concert with a high calcium peak. In Greenland, calcium is deposited in the northern hemisphere in spring with mineral dust, thus typically showing a distinct seasonal variability (Legrand and Mayewski 1997). This high calcium signal exceeds the seasonal peaks by far. It can be argued that here it might indicate the presence of tephra in the ice. However, as Abbot and Davies' (2012) summary of identified tephra layer horizons does not include tephra being detected at the equivalent depth in the NGRIP, GRIP or GISP2 ice core, this conclusion is not likely. Thus, this specific calcium event will need to be compared with investigations of tephra deposits in the EastGRIP ice core to obtain a conclusive result. In case of ash particles being found for this particular volcanic eruption, the geographic location of the eruption they originated from might be determined via chemical fingerprinting.
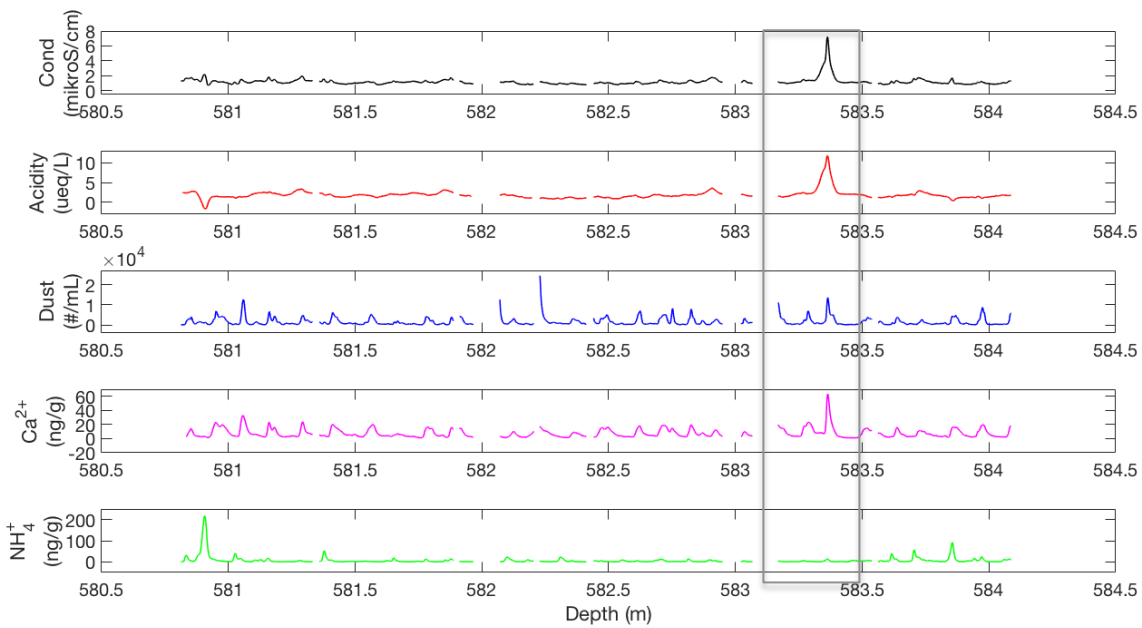
Figure 19: EastGRIP CFA data ranging from 580.5 m to 584.5 m depth, showcasing a big volcanic eruption. Electrolytic meltwater conductivity (black), acidity (red), dust (blue), calcium (purple) and ammonium (green) are shown from the top to the bottom panel. The event of interest is marked with a grey rectangle.
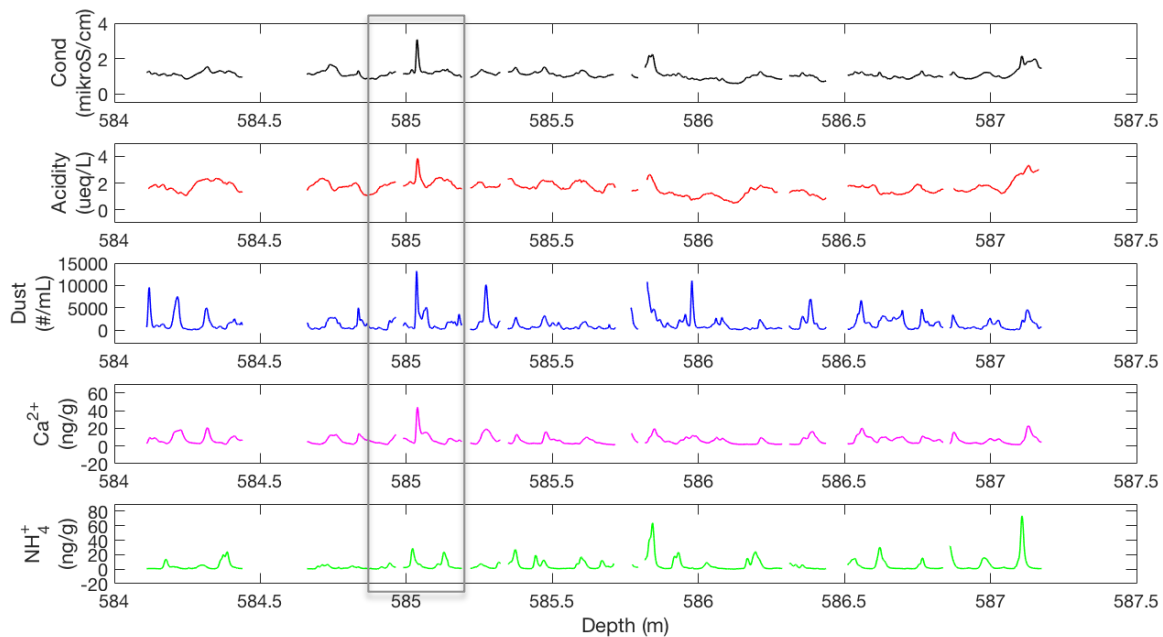
Figure 20: EastGRIP CFA data ranging from 584 m to 587.5 m depth, showcasing a possible melt event. Electrolytic meltwater conductivity (black), acidity (red), dust (blue), calcium (purple) and ammonium (green) are shown from the top to the bottom panel. The event of interest is marked with a grey rectangle.

Even though the acidity method shows performance issues, coupled with electrolytic meltwater conductivity, the data presented here gives indication of reasonable accuracy of volcanic activity at the time. The EastGRIP acidity measurements presented here together with electrolytic meltwater conductivity, dust, calcium and ammonium data

56

provides insight into the state of the climate and points towards interesting areas of future research with this data set.

6. Discussion

As part of this study, the optical dye method for acidity developed by Kjær et al. (2016) was optimized (sections 5.1 and 5.2). First, the instrument setup was changed as described in section 4.2. A simple descriptive comparison of a standard data run from both the original Copenhagen setup developed by Kjær et al. (2016) and the changed Berne setup shows that the latter outperforms the Copenhagen setup by means of a lower noise production. This difference results from the setup and the measurement principles used. Based on this comparison, the Copenhagen setup could be further optimized by adopting the Berne setup used during the EastGRIP measurement campaign 2019: Thus the implementation of a photosensor module coupled with a wavelength-specific LED and an optical-pass filter, enabling the detection at the peak wavelength of 589 nm, as well as temperature regulation could be tested.

Second, a dye test was conducted to investigate the leeway for optimizing the dye concentration of the reagent of the acidity method, aiming at further improving the performance of the method setup that was used for the first time during the EastGRIP measurement campaign 2019. Thereby eleven different dye concentrations (mg/mL) ranging from slightly weaker and stronger than what Kjær et al. (2016) determined as the optimal dye concentration for the Copenhagen setup were tested. The evaluated data showed a non-linear relationship between the sensitivity of the acidity method and the dye concentration with stronger sensitivities for stronger dye concentrations. Therein, the increase in sensitivity with increasing dye concentrations is diminishing; thus a negative exponential relationship is assumed for this saturation effect. On this basis, the optimal dye concentration should lie in an area of high sensitivity and where incremental changes in the concentrations do not lead to big changes in the response of the method. Both these requirements are true for strong dye concentrations. However, stronger dye concentrations also lower the light intensity detected by the instrument, as shown on the MilliQ baseline. As the baseline determines the area of the sensitivity of the method and under the assumption that the wearing out of the instrument induces a downward drift of the baseline over time, a dye concentration should be chosen that offers a baseline that is not too low. The trade-off between higher sensitivities, shorter response times, but lower baseline signals with stronger dye concentrations leads to the conclusion that the optimal dye concentration should thus be chosen from the mid-range concentrations tested in this experiment, equivalent to approximately 0.04 mg/mL to

0.06 mg/mL. Thus, this evaluation affirms the results of Kjær et al. (2016) proposing an optimal dye concentration of 0.05 mg/mL. However, the small data set available from this dye test introduces a high uncertainty of the results. Thus replicating this test while also narrowing the concentration steps of the different reagents tested would lead to more precise and reliable results.

The second part of this project investigated the method performance of the optimized Berne acidity setup based on the standard data for the period of the EastGRIP measurement campaign 2019 (section 5.3). The assessment of different calibration options showed a pronounced dependence of the calibration coefficients on how the calibration curve was produced: The calibration done with both the HCl and NaOH standards results in steeper slopes of the calibration curve. The steepest slopes thereby result from not forcing the calibration curve through zero. The two calibration methods only including the HCl standards both show less steep slopes of the calibration curves, with the least steep slopes occuring when not forcing the calibration curve through zero. Also, when the calibration curve is not forced through zero, a shift of the intercept towards zero after the standard concentrations were halved in the second week of the EastGRIP melting campaign 2019 can be observed. These discrepancies results from an observed non-linear relationship between the $-\log10(I/I_0)$ of the HCl and NaOH standard concentration. Thereto Kjær et al. (2016) hypothesize that the more acid and less acid standards exhibit a different strength of response to the two dyes. This difference is thus best represented with two separate linear regressions. Producing one linear gradient including both the NaOH and HCl standards, as done in this study, introduces a higher uncertainty for the subsequent calculation of the ice core concentrations. This result suggests that a calibration with incremental changes in the standard concentrations should be performed in the future in order to obtain a more precise calibration curve representing the real relationship between the absorption and the concentration of acidity. This would reduce uncertainties in the calculation of the acidity data from ice core CFA measurements.

Regarding the method performance over the course of the six and a half weeks of the EastGRIP measurement campaign 2019 three main issues can be outlined. The first two relate to the analysis of the calibration coefficients over time, whereas the third was observed in the processed ice core measurement data. First, both the week of the setup and the first few measurement days as well as the last week of the measurements exhibit

pronouncedly lower slopes of the calibration curves. However, as presumably a lot of variables were still changed in the week of the setup and an old stock reagent was used for these days, the data before the actual start of the measurement campaign (21 Jan 2019) might not be representative. And second, a fluctuation between lower and higher slopes of the calibration curves was observed. With the information available, the possibility of these shifts in the response of the method being induced by temperature changes, the LED, the photosensor module and the reagent was discussed in section 5.3. This study argues that neither of these system components would induce the observed deviances and drifts, but that these fluctuations could result from a combination of the variability in the standard preparation and the tubing of the acidity system. The latter might have induced small changes in the flow of the sample and dye reagent leading to changes in the mixing ratio of the two. Third, the processed ice core acidity measurement data showed a rather unstable baseline with a noteworthy linear downward drift of varying slope. With the acidity method being sensitive to the mixing ratio of the dye reagent and the sample, ageing of the lines might have caused this observed drift. Also, shifts in the baseline after the measurement runs were observed that might be induced by a change in another system.

Based on these results, this project suggests that a further investigation of these performance issues should test alternative tubing setups. As mentioned, the acidity method is highly sensitive to changes in the ratio of sample and dye concentration leading to drift induced by the ageing of the tubing as well as other more incalculable effects of new tubing "wearing in". A setup combining a larger tubing diameter with a more dilute reagent in order to compensate for the higher flow might lower the influence of the tubing on the acidity method performance (Email communication, Paul Travis Vallelonga, 6 Feb 2019).

The third part of this project presents and discusses an extract from the EastGRIP acidity record produced in the measurement campaign 2019 in comparison with further CFA data (section 5.4): meltwater electrolytic conductivity, dust, calcium and ammonium data. This provides insight into the state of the climate at that time with regards to volcanic activity. Thereby, during the EastGRIP measurement campaign 2019, a total of approximately 554 m of the EastGRIP ice core was melted from a depth of 350.35 m to 904.75 m. Calculated with a preliminary time scale, these depths correspond to a time range spanning roughly from 3 ky to further than 7.6 ky before

2000 CE. As the NEEM brittle ice zone ranges from around 3 ky to 9 ky BP (Neff 2014), the EastGRIP CFA data from the 2019 measurement campaign thus fills in the gap of discontinued data of the NEEM ice core. The data produced can be further used to investigate volcanic activity, advancing the completion of the climate record of the mid-Holocene period. At the same time, the obtained CFA data can be used for further assessments of the acidity method performance, such as for example the impact of dust on the acidity measurements. As the ice from glacial periods contains much higher dust loads than the ice from the Holocene, an assessment of this kind is of high importance in order to estimate the application of the continuous optical dye acidity method for coming EastGRIP – as well as other – CFA measurement campaigns.

7. Conclusion

The results of this study and the CFA acidity data obtained from the EastGRIP ice core contribute to the climate record of past volcanic activity and subsequently facilitate the understanding of past changes of the climate as a result to volcanic forcing. In the context of anthropogenic climate change this is of high importance, as volcanic eruptions are the dominant cause for natural climate change on the annual and multi-decadal time scale and explain much of the climate variability in the pre-industrial area of the last millennium (IPCC 2013c). To this end, scientific knowledge on past natural climate fluctuations caused by volcanism facilitates the detection of global warming since industrialization and helps improve model projections of anthropogenic climate change.

This study aimed at investigating volcanic activity in the EastGRIP ice core data with an optimized acidity technique as a way of contributing to the completion of the CFA climate proxy record of the mid-Holocene period. In this process, three main objectives have been obtained: First, the optimization of the continuous optical dye method for acidity increased the signal to noise ratio and found an optimized dye concentration range of 0.04 mg/mL to 0.06 mg/mL, affirming the results of Kjær et al. (2016) proposing an optimal dye concentration of 0.05 mg/mL (see section 5.2).

Second, the evaluation of the standard data of the EastGRIP measurement campaign 2019 emphasizes that the optimization of the acidity detection system led to a satisfactory performance of the detection system overall (see section 5.3). An observed variability in the sensitivity over the course of the measurement campaign, however, pinpoints a possible leeway for future optimization of the method by changing the tubing used for the acidity setup. On the basis of the assessment of the method performance over the course of the EastGRIP measurement campaign 2019 it can thereby be concluded that the EastGRIP acidity data obtained as part of this study is of reasonable quality and can thus be trusted in future investigations of climatic events.

To this end, and thereby meeting the third objective of this study, the EastGRIP measurement data for the acidity, combined with CFA meltwater electrolytic conductivity, dust, calcium and ammonium data showcases selected indications for volcanic activity during in the EeastGRIP data in the time period of approximately 3 ky to further than 7.6 ky before 2000 CE (see section 5.4).

Literature

Abbott, P.M. and Davies, S.M. (2012) 'Volcanism and the Greenland ice-cores: the tephra record', *Earth-Science Reviews*, 115(3), 173–191, available: https://doi.org/10.1016/j.earscirev.2012.09.001.

Anklin, M., Barnola, J.-M., Schwander, J., Stauffer, B. D. Raynaud, D. (1995) 'Processes affecting the CO_2 concentrations measured in Greenland ice', *Tellus*, 47(4), 461–470, avialable: https://doi.org/10.1034/j.1600-0889.47.issue4.6.x.

Bierman, P.R., Shakun, J.D., Corbett, L.B., Zimmerman, S.R., and Rood, D.H. (2016) 'A persistent and dynamic East Greenland Ice Sheet over the past 7.5 million years', *Nature*, 540(7632), 256–260I, available: http://dx.doi.org.ep.fjernadgang.kb.dk/10.1038/nature20147.

Bigler, M. (2000) '*Entwicklung und Anwendung einer neuen Methode zur kontinuerlichen, hochaufgelösten Messung der Sulfatkonzentration an alpinen und polaren Eisbohrkernen*', Diplomarbeit der Philosophisch-naturwissenschaftlichen Falkultät der Universität Bern, available: http://citeseerx.ist.psu.u/viewdoc/download?doi=10.1.1.219.4750&rep=rep1&type=pdf [30 May 2019].

Bigler et al. Bigler, M., Svensson, A., Kettner, E., Vallelonga, P., Nielsen, M.E. and Steffensen, J.P. (2011), 'Optimization of High-Resolution Continuous Flow Analysis for Transient Climate Signals in Ice Cores', *Environmental Science & Technology,* 45(10), 4483-4489, available: https://doi-org.ep.fjernadgang.kb.dk/10.1021/es200118j.

Bonne, J., Steen-Larsen, H.C., Risi, C., Werner, M., Sodemann, H., Lacour, J., Fettweis, X., Cesana, G., Delmotte, M., Cattani, O., Vallelonga, P., Kjær, H.A., Clerbaux, C., Sveinbjörnsdóttir, Á.E. and Masson-Delmotte, V. (2015) 'The summer 2012 Greenland heat wave: In situ and remote sensing observations of water vapor isotopic composition during an atmospheric river event', *Journal of Geophysical Research: Atmospheres*, 120, 2970–2989, available: https://doi.org/10.1002/2014JD022602.

Bradley, R.S. (2015) Paleoclimatology: Reconstructing Climates of the Quaternary, ed. 3, Elsevier Inc.

Chemistry LibreTexts (2019a) *The Beer-Lambert Law*, available: https://chem.libretexts.org/Bookshelves/Physical_and_Theoretical_Chemistry_Textbook_Maps/Supplemental_Modules_(Physical_and_Theoretical_Chemistry)/Spectroscopy/Electronic_Spectroscopy/Electronic_Spectroscopy_Basics/The_Beer-Lambert_Law [29 May 2019].

Chemistry LibreTexts (2019b) *Titrations*, available: https://chem.libretexts.org/Bookshelves/General_Chemistry/Book%3A_General_Chemistry_Supplement_(Eames)/Chemistry_Calculations/Titrations [29 May 2019].

Cuffey, K.M. and Paterson, W.S.B. (2010) *The Physics of Glaciers*, ed. 4, USA: Elsevier Inc.

EastGRIP (2019) *About EastGRIP*, available: https://www.eastgrip.org/About.html [30 May 2019].

Fischer, E.M. (2006) 'Climate response to tropical eruptions', in *Pages News,* 13(3), available: doi:10.3929/ethz-b-000022496.

Fischer, H., Siggard-Andersen, M.-L., Ruth, U., and Röthlisberger, R.W.E. (2007) 'Glacial/interglacial changes in mineral dust and sea-salt records in polar ice cores:

Sources, transport, and deposition', *Reviews of Geophysics,* 45(1), RG1002, available: https://doi.org/10.1029/2005RG000192.

Hammer, C.U., Clausen, H.B. and Dansgaard, W. (1980) 'Greenland ice sheet evidence of post-glacial volcanism and its climatic impact', *Nature,* 288, 230–235, available: https://doi.org/10.1038/288230a0.

IPCC (2018) 'Summary for Policymakers', in Masson-Delmotte, V., Zhai, P., Pörtner, H.-O., Roberts, D., Skea, J., Shukla, P.R., Pirani, A., Moufouma-Okia, W., Péan, C., Pidcock, R., Connors, S., Matthews, J.B.R., Chen, Y., Zhou, X., Gomis, M.I., Lonnoy, E., Maycock, T., Tignor, M. and Waterfield, T. eds., *Global Warming of 1.5°C. An IPCC Special Report on the impacts of global warming of 1.5°C above pre-industrial levels and related global greenhouse gas emission pathways, in the context of strengthening the global response to the threat of climate change, sustainable development, and efforts to eradicate poverty,* Geneva, Switzerland: World Meteorological Organization, 32 pp.

Kaufmann, P.R., Federer, U., Hutterli, M.A., Bigler, M., Schüpbach, S., Ruth, U., Schmitt, J. and Stocker, T.F. (2008) 'An Improved Continuous Flow Analysis System for High-Resolution Field Measurements on Ice Cores', *Environmental Science & Technology*, 42(21), 8044–8050, available: https://doi-org.ep.fjernadgang.kb.dk/10.1021/es8007722.

Kjær, H.A. (2014) *Continuous Chemistry in Ice Cores: Phosphorus, pH and the Photolysis of Humic Like Substances,* thesis (PhD), The Niels Bohr Institute of Science, University of Copenhagen.

Kjær, H.A., Vallelonga, P., Svensson, A., Kristensen, M.E.L., Tibuleac, C., Winstrup, M. and Kipfstuhl, S. (2016) 'An Optical Dye Method for Continuous Determination of Acidity in Ice Cores', *Environmental Science & Technology,* 50(19), 10485–10493, available: https://doi.org/10.1021/acs.est.6b00026.

Kreuz, K.J. and Koffman, B.G. (2013) 'Ice core methods: Glaciochemistry', in Elias, S.A., ed., *Encyclopedia of Quaternary Science,* ed. 2, Amsterdam: Elsevier, 326–333.

Langway, C.C (2008) 'The history of early polar ice cores', *Cold Regions Science and Technology,* 101–117, available: http://www.iceandclimate.nbi.ku.dk/about_centre/history/Langway_2008_The_history_of_early_polar_ice_cores.pdf [30 May 2019].

Legrand, M. and Mayewski, P. (1997) 'Glaciochemistry of polar ice cores: A review', *Reviews of Geophysics*, 35(3), 219–243, available: https://doi.org/10.1029/96RG03527.

Legrand, M.R., Aristarain, A.J. and Delmas, R. J. (1982) 'Acid titration of polar snow', *Analytical Chemistry*, 54(8), 1336–1339, available: https://doi-org.ep.fjernadgang.kb.dk/10.1021/ac00245a020.

Masson-Delmotte, V., Schulz, M., Abe-Ouchi, A., Beer, J., Ganopolski, A., González Rouco, J.F., Jansen, E., Lambeck, K., Luterbacher, J., Naish, T., Osborn, T., Otto-Bliesner, B., Quinn, T., Ramesh, R., Rojas, M., Shao, X. and Timmermann A. (2013b) 'Information from Paleoclimate Archives', in Stocker, T.F., Qin, D., Plattner, G.-K., Tignor, M., Allen, S.K., Boschung, J., Nauels, A., Xia, Y., Bex, V. and Midgley, P.M. eds., *Climate Change 2013: The Physical Science Basis. Contribution of Working Group I to the Fifth Assessment Report of the Intergovernmental Panel on Climate Change*, Cambridge, United Kingdom and New York, USA: Cambridge University Press, 383–464, (cited as: IPCC 2013b).

Moore, J. and Paren, J. (1987) 'A NEW TECHNIQUE FOR DIELECTRIC LOGGING OF ANTARCTIC ICE CORES', *Journal de Physique Colloques*, 48(C1), C1-155–C1-160, available: https://doi.org/10.1051/jphyscol:1987123.

Myhre, G., Shindell, D., Bréon, F.-M., Collins, W., Fuglestvedt, J., Huang, J., Koch, D., Lamarque, J.-F., Lee, D., Mendoza, B., Nakajima, T., Robock, A., Stephens, G., Takemura, T. and Zhang, H. (2013c) 'Anthropogenic and Natural Radiative Forcing', in Stocker, T.F., Qin, D., Plattner, G.-K., Tignor, M., Allen, S.K., Boschung, J., Nauels, A., Xia, Y., Bex, V. and Midgley, P.M. eds., *Climate Change 2013: The Physical Science Basis. Contribution of Working Group I to the Fifth Assessment Report of the Intergovernmental Panel on Climate Change,* Cambridge, United Kingdom and New York, USA: Cambridge University Press, 659–740, (cited as: IPCC 2013c)

Neff, P.D. (2014) 'A review of the brittle ice zone in polar ice cores', *Annals of Glaciology*, 55(68), 72–82, available: https://doi.org/10.3189/2014AoG68A023.

Oeschger, H., Neftel, A., Staffelbach, T. and Stauffer, B. (1988) 'The Dilemma of the Rapid Variations in CO_2 in Greenland Ice Cores (Abstract)', *Annals of Glaciology,* 10, 215–216, available: https://doi.org/10.3189/S0260305500004626.

Parrenin, F., Petit, J.R., Masson-Delmotte, V., Wolff, E., Basile-Doelsch, I., Jouzel, J., Lipenkov, V., Rasmussen, S.O., Schwander, J., Severi, M., Udisti, R., Veres, D., and Vinther, B.M. (2012) 'Volcanic synchronisation between the EPICA Dome C and Vostok ice cores (Antarctica) 0–145 kyr BP', *Climate of the Past*, 8, 1031–1045, available: https://doi.org/10.5194/cp-8-1031-2012.

Pasteris, D.R., McConnell, J.R. and Edwards, R. (2012) 'High-resolution, Continuous Method for Measurement of Acidity in Ice Cores', *Environmental Science & Technology*, 46(3), available: https://doi-org.ep.fjernadgang.kb.dk/10.1021/es202668n.

Richardson, K., Steffen, W. and Liverman, D. eds. (2011) *Climate Change: Global Risks, Challenges and Decisions,* New York: Cambridge University Press.

Robock, A. (2000) 'Volcanic eruptions and climate', *Reviews of Geophysics,* 38(2), 191–219, available: https://doi.org/10.1029/1998RG000054.

Röthlisberger, R., Bigler, M., Hutterli, M., Sommer, S., Stauffer, B., Junghans, H.G. and Wagenbach, D. (2000) 'Technique for Continuous High-Resolution Analysis of Trace Substances in Firn and Ice Cores', *Environmental Science & Technology*, 34(2), 338–342, available: https://doi-org.ep.fjernadgang.kb.dk/10.1021/es9907055.

Schaefer, J.M., Finkel, R.C., Balco, G., Alley, R.B., Caffee, M.W., Briner, J.P., Jason, P., Young, N.E., Gow, A.J. and Schwartz, R. (2016) 'Greenland was nearly ice-free for extended periods during the pleistocene', *Nature* 540(7632), 252–255, available: http://dx.doi.org.ep.fjernadgang.kb.dk/10.1038/nature20146.

Schüpbach, S., Fischer, H., Bigler, M., Erhardt, T., Gfeller, G., Leuenberger, D., Mini, O., Mulvaney, R., Abram, N. J., Fleet, L., Frey, M.M., Thomas, E., Svensson, A., Dahl-Jensen, D., Kettner, E., Kjaer, H., Seierstad, I., Steffensen, J.P., Rasmussen, S.O., Vallelonga, P., Winstrup, M., Wegner, A., Twarloh, B., Wolff, K., Schmidt, K., Goto-Azuma, K., Kuramoto, T., Hirabayashi, M., Uetake, J., Zheng, J., Bourgeois, J., Fisher, D., Zhiheng, D., Xiao, C., Legrand, M., Spolaor, A., Gabrieli, J., Barbante, C., Kang, J.-H., Hur, S.D., Hong, S.B., Hwang, H.J., Hong, S., Hansson, M., Iizuka, Y., Oyabu, I., Muscheler, R., Adolphi, F., Maselli, O., McConnell, J. and Wolff, E.W. (2018) 'Greenland records of aerosol source and atmospheric lifetime changes from the Eemian to the Holocene', *Nature Communications*, 1476(2018), 2041–1723, available: https://doi.org/10.1038/s41467-018-03924-3.

Sigg, A., Fuhrer, K., Anklin, M., Staffelbach, T. and Zurmuehle, D. (1994) 'A continuous analysis technique for trace species in ice cores', *Environmental Science & Technology*, 28(2), 204–209, available: https://doi-org.ep.fjernadgang.kb.dk/10.1021/es00051a004.

Stocker, T.F., Qin, D., Plattner, G.-K., Alexander, L.V., Allen, S.K., Bindoff, N.L., Bréon, F.-M., Church, J.A., Cubasch, U., Emori, S., Forster, P., Friedlingstein, P., Gillett, N., Gregory, J.M., Hartmann, D.L., Jansen, E., Kirtman, B., Knutti, R., Krishna Kumar, K., Lemke, P., Marotzke, J., Masson-Delmotte, V., Meehl, G.A., Mokhov, I.I., Piao, S., Ramaswamy, V., Randall, D., Rhein, M., Rojas, M., Sabine, C., Shindell, D., Talley, L.D., Vaughan, D.G. and Xie, S.-P. (2013a) 'Technical Summary', in Stocker, T.F., Qin, D., Plattner, G.-K., Tignor, M., Allen, S.K., Boschung, J., Nauels, A., Xia, Y., Bex, V. and Midgley, P.M. eds., *Climate Change 2013: The Physical Science Basis. Contribution of Working Group I to the Fifth Assessment Report of the Intergovernmental Panel on Climate Change*, Cambridge, United Kingdom and New York, USA: Cambridge University Press, (cited as: IPCC 2013a).

Svensson, A., Andersen, K.K., Bigler, M., Clausen, H.B., Dahl-Jensen, D., Davies, S.M., Johnsen, S.J., Muscheler, R., Parrenin, F., Rasmussen, S.O., Röthlisberger, R., Seierstad, I., Steffensen, J.P. and Vinther, B. M. (2008) 'A 60 000 year Greenland stratigraphic ice core chronology', *Climate of the Past,* 4, 47–57, available: https://doi.org/10.5194/cp-4-47-2008.

Svensson, A. (2014) ‚Ice cores', in Rink W. and Thompson, J. eds., *Encyclopedia of Scientific Dating Methods,* Dordrecht: Springer, available: https://doi.org/10.1007/978-94-007-6326-5.

Timmreck, C. (2012) 'Modeling the effects of large explosive volcanic eruptions', *WIREs Climate Change*, 3(6), 545–564, available: https://doi.org/10.1002/wcc.192.

Vinther, B.M., Clausen, H.B., Johnsen, S.J., Rasmussen, S.O., Andersen, K.K., Buchardt, S. L., Dahl-Jensen, D., Seierstad, I.K., Siggaard-Andersen, M.-L., Steffensen, J.P., Svensson, A. M., Olsen, J., and Heinemeier, J. (2006) 'A synchronized dating of three Greenland ice cores throughout the Holocene', *Journal of Geophysical Research,* 111(D13), available: https://doi.org/10.1029/2005JD006921.

Wolff, E.W., William, D., Moore, J.C. and Paren, J.G. (1997) 'Factors Controlling the Electrical Ionductivity of ice from the Polar Regions − A summary', *The Journal of Physical Chemistry B*, 101(32), 6090–6094, available: https://doi.org/10.1021/jp9631543.

Wolff, E.W., Chappellaz, J., Blunier, T., Rasmussen, S.O. and Svensson, A. (2010) 'Millennial-scale variability during the last glacial: The ice core record', *Quaternary Science Reviews*, 29(21–22), 2828–2838, available: https://doi.org/10.1016/j.quascirev.2009.10.013.

Declaration

I hereby declare that this thesis complies with good scientific practice and all university regulations.

Copenhagen, 31 May 2019

Mirjam Martina Läderach